UNIVERSITY OF TEXAS AT ARLINGTON

MASTERS THESIS

Multiple Coulomb Scattering In the LArIAT Detector

Author:
Dalton SESSUMES

Supervisor:
Dr. Jonathan ASAADI
Committee:
Dr. Kaushik De
Dr. Jaehoon Yu

A thesis submitted in fulfillment of the requirements
for the degree of Master of Science in Physics

in the

High Energy Physics Group
Department of Physics

December, 2018

Declaration of Authorship

I, Dalton SESSUMES, declare that this thesis titled, "Multiple Coulomb Scattering In the LArIAT Detector" and the work presented in it are my own. I confirm that:

- This work was done wholly or mainly while in candidature for a research degree at this University.

- Where any part of this thesis has previously been submitted for a degree or any other qualification at this University or any other institution, this has been clearly stated.

- Where I have consulted the published work of others, this is always clearly attributed.

- Where I have quoted from the work of others, the source is always given. With the exception of such quotations, this thesis is entirely my own work.

- I have acknowledged all main sources of help.

- Where the thesis is based on work done by myself jointly with others, I have made clear exactly what was done by others and what I have contributed myself.

Signed:

_____

Date:

_____

"We didn't reinvent the circus. We repackaged it in a much more modern way."

UNIVERSITY OF TEXAS AT ARLINGTON

Abstract

Dr. Jonathan Asaadi
Department of Physics

Master of Science in Physics

Multiple Coulomb Scattering In the LArIAT Detector

by Dalton SESSUMES

LArIAT is a liquid argon time projection chamber (LArTPC) that aims to measure an interaction process known as multiple coulomb scattering, which describes the millions of scatters a particle experiences as it passes through a material due to its interactions with the nuclei of the material. This work presents a characterization of charged particle multiple coulomb scattering as a function of incoming momentum and particle type. Employing data collected by the LArIAT experiment and single particle Monte Carlo reconstruction, we measure the scattering angles of single particle tracks at specified momentum ranges. The scattering angles are modeled as an exponential distribution with a slope parameter that is used to calculate σ^{HL}, a value that is related to the particle's momentum via the Highland Formula. The results of the data and simulation measurement are compared against the Highland Formula and fit to a tuned variation of the Highland formula to extract a new particle-dependent, data-driven parameter for various particles in liquid argon. This method and its results are compared to the standard Highland formula and previous measurements in argon performed by the MicroBooNE experiment. This cross-check provides a more accurate understanding of K^+, π^+, μ^+, and p scattering behavior in LArTPC detectors and highlights a discrepancy between Monte Carlo reconstruction and data.

Acknowledgements

Contents

List of Figures

List of Tables

List of Abbreviations

LAr   Liquid **Ar**gon
LArIAT   Liquid **Ar**gon **I**n **A** **T**estbeam
LArTPC   Liquid **Ar**gon **T**ime **P**rojection **C**hamber
TPC   **T**ime **P**rojection **C**hamber
MCS   **M**ultiple **C**oulomb **S**cattering
FTBF   **F**ermilab **T**est **B**eam **F**acility
ArgoNeuT **Argo**n **Neu**trino **T**eststand
MicroBooNE **Micro**-**Boo**ster **N**eutrino **E**xperiment
WC2TPC   **W**ire **C**hamber **to** **T**ime **P**rojection **C**hamber
SNU   **S**olar **N**eutrino **U**nit
SNO   **S**udbury **N**eutrino **O**bservatory
HL   **H**igh**L**and Formula
THL   **T**uned **H**igh**L**and Formula
MC   **M**onte **C**arlo

Physical Constants

Speed of light	$c = 2.997\,924\,58 \times 10^8 \,\mathrm{m\,s^{-1}}$ (exact)
Mass of kaon	$m_{k+} = 493.7 \,(\mathrm{MeV}/c^2)$ (approx)
Mass of muon	$m_\mu = 105.658 \,(\mathrm{KeV}/c^2)$ (approx)
Mass of proton	$m_p = 938.272 \,(\mathrm{KeV}/c^2)$ (approx)
Mass of pion	$m_\pi = 139.570 \,(\mathrm{KeV}/c^2)$ (approx)
Highland constant	$m_\epsilon = 0.038$
Nominal Highland coefficient	$S_2 = 13.6 \,(\mathrm{MeV})$
Track length	$L_o = .14 \,(\mathrm{m})$
Radiation length (in argon)	$X_o = .14 \,(\mathrm{m})$
Solar Neutrino Unit	$SNU = 10^{-36}(\mathrm{captures/target\ atom \cdot sec})$

List of Symbols

p Proton particle
κ Kaon particle
μ Muon particle
π Pion particle
ρ Momentum
θ_{3D} 3D scattering angle   (rad)
σ_0 Root-mean-squared width   (cm^2)
χ^2 The reduced chi-squared statistic

Dedicated to the artists of the world for meeting our pursuits in science with equal pursuits in spirit.

Chapter 1

Introduction

1.1 Neutrino Physics

Neutrinos were first proposed in a letter dating back to 1930 in which W. Pauli outlined what he described to be a "desparate remedy" to the apparent nonconservation of energy in radioactive β-decays and the contradictory spin statistics of N^{14} and Li^6 nuclei[1]. The Proton-Electron model predicts that the β-decay of a nucleus (A, Z) emits an electron in the nuclear transition $(A, Z) \rightarrow (A, Z + 1) + e^-$. Conservation of energy and momentum within this model show that an ejected electron would have a fixed kinetic energy $Q = (m_{A,Z} - m_{A,Z+1}) - m_e$. However, experiments showed that the kinetic energy occured in a continuous spectrum with Q as an end-point. The 1927 Ellis and Wooster calorimetric β-decay experiment[2] then showed that the predicted energy released by Radium E (also known as bismuth-210) decaying into Polonium was four times larger than the detected energy, motivating Pauli's proposal for a new, electrically neutral particle which is emitted in the β-decay together with the electron and was not detected in experiments.

Originally dubbed the "neutron", this particle changed the β-decay to a three-body process such that $(A, Z) \rightarrow (A, Z + 1) + e^- + ''n''$. In this process, the released energy is distributed between the electron and the "neutron", giving rise to a continuous electron energy spectrum. Pauli postulated that the "neutrons" had spin 1/2 and mass on the same order of magnitude as the
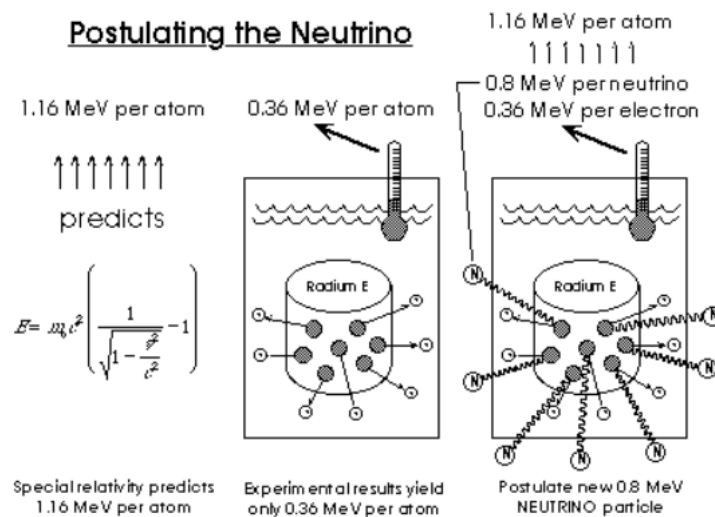
FIGURE 1.1: The Ellis and Wooster calorimetric β-decay experiment showing the disparity between predicted and measured energy values in the β-decay of Radium E to Polonium.

electron mass. The theory of nucleic β-decay was more fully developed by E. Fermi in 1934, who then renamed Pauli's "neutron" *the neutrino*[3].

Being a chargeless and nearly massless particle, neutrinos are incredibly difficult to detect. In 1950, F. Reines and C. Cowan designed an experiment to verify the particle's existence using a detector in close proximity to a nuclear reactor. The machine expected to produce neutrino fluxes on the order of 10^{12}-10^{13} neutrinos per second per cm^2, nearly seven orders of magnitude higher than common radioactive sources. These neutrinos would be incident on Reines and Cowan's experiment causing inverse β-decay events which produce neutrons and positrons in the reaction $\bar{\nu}_e + p \rightarrow n + e^+$. The positrons produced by this reaction quickly pair-annihilate with nearby electrons, giving off two 0.5 MeV gamma rays in opposite directions that are easily detectable. To confirm the reaction was in fact neutrino-induced, Reines and Cowan employed liquid scintillator saturated with dissolved cadmium chloride that produced one pulse in response to the annihilation product gamma photons and a second pulse upon capture of the moderated neutron on the cadmium atom and emission of a third gamma ray in the reaction

$n +^{108} Cd \rightarrow^{109} Cd^* \rightarrow^{109} Cd + \gamma$. Their setup prescribed a distinctive signature for the neutrino reaction: a pair of simultaneous gamma rays followed by another gamma ray after a 5 μs delay. In 1956, Reines and Cowan achieved an experimental cross-section measurement of $6.3x10^{-44} \pm 0.315x10^{-44}$ cm^2, which when compared to their predicted $6x10^{-44}$ cm^2, was enough to confirm the existence of the neutrino[4][5].

The next significant problem in neutrino physics began in 1965 with R. Davis and J. Bahcall's Homestake Experiment[6]. This experiment was designed to measure the flux of solar neutrinos and prove that the sun runs on thermonuclear power. Based on the inverse β-decay reaction $\nu_e +^{37} Cl \rightarrow^{37} Ar + e^-$, Davis used two 500 gallon tanks of perchlorethylene, C_2Cl_4, 2300 feet deep inside a limestone mine equipped with agitators and an auxiliary system to measure the extracted ^{37}Ar content. The number of ^{37}Ar atoms extracted from the detector was determined by observing their decay in a miniature gas-filled proportional counter. This type of counter produced a pulse proportional to the 2.8 keV charge liberated by an electron passing through the counter and thus to the energy lost in the counter gas by the electron. Davis found that the combined result of 108 extractions was a solar neutrino-induced ^{37}Ar production rate of 2.56 $\pm$ 0.l6 (statistical) $\pm$ 0.16 (systematic) SNU (1 SNU $\approx 10^{-36}$ capture per second per target atom). This count was less than 1/3 of the 9.3 $\pm$ 1.3 SNU production rate theorized by Bahcall, and hence gave birth to the *solar neutrino problem*[7][8].

The solar neutrino problem was repeatedly verified by multiple experiments [9][10][11], each observing between 1/3 and 1/2 of the predicted solar neutrino flux. Members of the scientific community put forth several possible solutions:

- All the previous experiments were wrong;

- The predicted solar neutrino fluxes of the Standard Solar Model were wrong;

- Solar neutrinos change flavor from ν_e to ν_μ and/or ν_τ;

- Something else happens to the solar neutrinos (e.g. ν_e mix with another flavor of neutrinos that is yet to be detected).

The most intriguing of these solutions was the possibility that neutrinos might change flavor as they travel to Earth. If this were true, it would also imply the significant requirement that solar neutrinos have non-zero rest mass. In 1998, the Super-Kamiokande experiment provided strong evidence for muon neutrinos changing into tau neutrinos. They found that the through-going upward muon flux and the ratio of stopping to through-going fluxes as a function of zenith angle both deviated significantly from expectation based on the absence of neutrino oscillations, but they agreed with expectation assuming two-flavor $\nu_\mu \rightarrow \nu_\tau$ oscillations. The Super-Kamiokande experiment also provided a solar neutrino cross section by counting neutrino scatters in water, which offered sensitivity to electron neutrinos as well as a slight sensitivity to other flavors[12]. In 2001, the SNO collaboration published their findings for a neutrino cross section that was made by counting neutrino scatters in heavy water, which has no sensitivity to neutrino flavors other than electron neutrinos. The discrepancy between the SNO solar neutrino count and the Super-Kamiokande neutrino count lent further evidence to the theory of neutrino oscillations. One year later, SNO published data from an experiment based on neutral-current reactions that allowed electron, muon, and tau neutrinos to scatter on an equal footing. The data showed that the sum total of solar electron, muon, and tau neutrinos equaled the predicted count to within 5.3 standard deviations, thus verifying the theory of neutrino oscillations and putting the solar neutrino problem to rest[13].

Since the early days of neutrino physics, we have significantly focused our knowledge into a few key characteristics. Neutrinos are leptons with no electrical charge that interact only via the weak subatomic force and gravity. Weak interactions create neutrinos in one of three known flavors: electron

neutrinos, muon neutrinos, or tau neutrinos determined by the corresponding lepton involved in the interaction. A neutrino created with a specific flavor is in an associated specific quantum superposition of all three mass states. As a result, neutrinos oscillate between different flavors in flight. The masses of each of the three flavors are believed to be less than one millionth of the mass of an electron, although we only have some neutrino mass-squared differences[14][15]. There is intense research activity involving neutrinos, with goals that include the ordering of the three neutrino mass values, the measurement of the degree of charge-parity violation in the leptonic sector (leading to leptogenesis), and searches for evidence of physics beyond the Standard Model—our classification model for the known fundamental forces and elementary particles—such as neutrinoless double β-decay, which would be evidence for violation of lepton number conservation.

In order to answer these questions in neutrino physics, high accuracy and high resolution data is needed to continue pushing the development of ever more precise neutrino detectors. In the next section, I will describe some different types of neutrino detectors used in modern neutrino experiments.

1.2 Neutrino Detectors

In modern neutrino physics, there are 4 major types of neutrino detectors commonly used. These include magnetized iron/steel calorimeters, Cherenkov detectors, liquid scintillators, and most pertinent to this paper, time projection chambers. Each type has 3 major components in common: a particle beam, an interaction medium, and an electronic readout system.

An example of a modern iron calorimeter is the proposed iron calorimeter (ICAL) experiment at the India-based Neutrino Observatory (INO). The goal of the first phase of this experiment is to measure atmospheric neutrinos and antineutrinos produced by interactions of cosmic rays in the Earth's
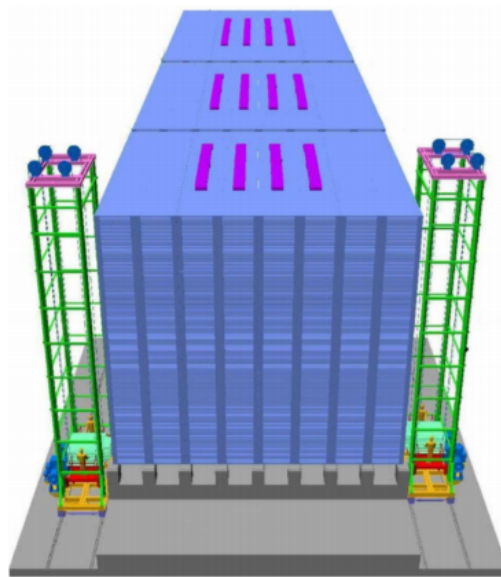
FIGURE 1.2: Schematic view of the 50 kt iron calorimeter detector ICAL at the INO site. The detector consists of 3 modules each having 140 layers of magnetized iron plates of 6 cm thickness. The 2.5 cm gaps between the plates house the resistive plate chambers.

atmosphere. INO will use an iron calorimeter (ICAL) constructed in horizontal layers sandwiched with the detector material that will trigger whenever a charged particle passes through it. The direction and the energy of the original incoming neutrino that caused the interaction can then be determined. By winding coils solenoidally around the iron plates and passing current through them, a uniform magnetic field can be created inside the detector. The charged particles bend in the magnetic field with oppositely charged particles bending in opposite directions. This will not only allow a charge identification of the emitted particle, but it also will provide a good measurement of its momentum. The site for the INO has been identified, and the construction is expected to start soon. Meanwhile, the design for the ICAL detector, including the design of its modules, magnet coils, active detector elements, and associated electronics, has been underway over the past decade[16].

The present generation water Cherenkov detector is Super-Kamiokande
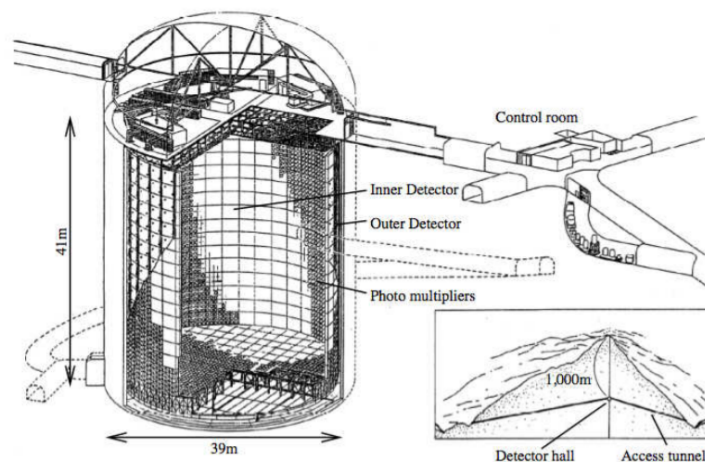
FIGURE 1.3: Diagram of the Super-Kamiokande detector. The detector is mainly comprised of two segments, the inner and outer detectors. The boundary between the two segments is defined by a cylindrical scaffold used to mount photomultiplier tubes and optically separate the segments.

(SuperK), whose results dominate our understanding of atmospheric neutrinos [17]. Cherenkov detectors function by holding a large volume of liquid that acts as a dielectric medium. As particles reach speeds faster than the phase velocity of light in that medium, they release a "sonic boom" of electromagnetic radiation known as Cherenkov radiation. Arrays of photomultiplier tubes around the dielectric medium then collect the electromagnetic signals for processing[18]. SuperK began taking data in 1996 and has a total mass of 50 kilotons. SuperK uses 11,146 photomultiplier tubes, each with a 20 inch diameter. An outer detector surrounds the inner detector with 2 meter thickness of water, equipped with 1885 photomultiplier tubes, each with an 8 inch diameter and wavelength-shifting plates. The fiducial volume for neutrino vertices is 2 meters from the plane of photomultiplier tubes, resulting in a 22.5 kiloton mass. The large mass and photocathode coverage allow for high statistics and detailed studies of atmospheric neutrinos[19][20]. Previous significant results of the Super-Kamiokande experiment include the first unambiguous evidence of neutrino oscillation in atmospheric neutrinos

[21], confirmation of the solar neutrino flux deficit and proof that solar neutrinos truly come from the sun using real-time observations[22], the first measurement of the solar neutrino energy spectrum above 5 MeV[23], and the world's highest lower limits on partial lifetimes for nucleon decay modes such as $p \to e^+ \pi^0$ and $p \to \nu K^+$[24][25].
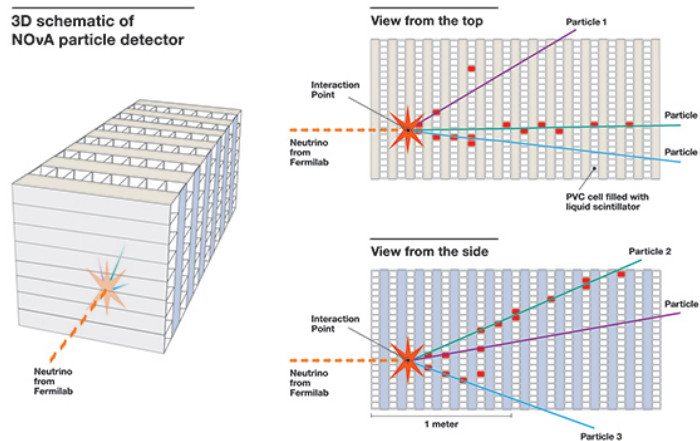
FIGURE 1.4: Leftmost portion shows a 3D view of the NOνA detector. Middle portion shows a neutrino interaction in both views of the detector. Rightmost portion shows a PVC plastic cell containing liquid scintillator and wavelength-shifting fiber to collect scintillating light and routes the light to an avalanche photodiode.

The NOνA experiment uses two variations of liquid scintillator detectors: a 300 metric-ton near detector at Fermilab and a much larger 14 metric-kiloton far detector in Minnesota just south of the U.S.-Canada border. The detectors are made up of 344,000 cells of extruded, highly reflective plastic PVC filled with liquid scintillator. Each cell in the far detector measures 3.9 cm wide, 6.0 cm deep and 15.5 meters long. Neutrinos that strike an atom in the liquid scintillator release a burst of charged particles. As these particles come to rest in the detector, they are collected using wavelength-shifting fibers connected to photo-detectors. Scientists can determine what kind of neutrino caused the interaction and what its energy was via its unique track shape and energy deposition[26]. The goals of the NOνA experiment include isolating the oscillation of muon neutrinos to electron neutrinos, finding the

ordering of the neutrino masses, and characterizing the asymmetry between matter and antimatter by observing charge-parity violation in action.
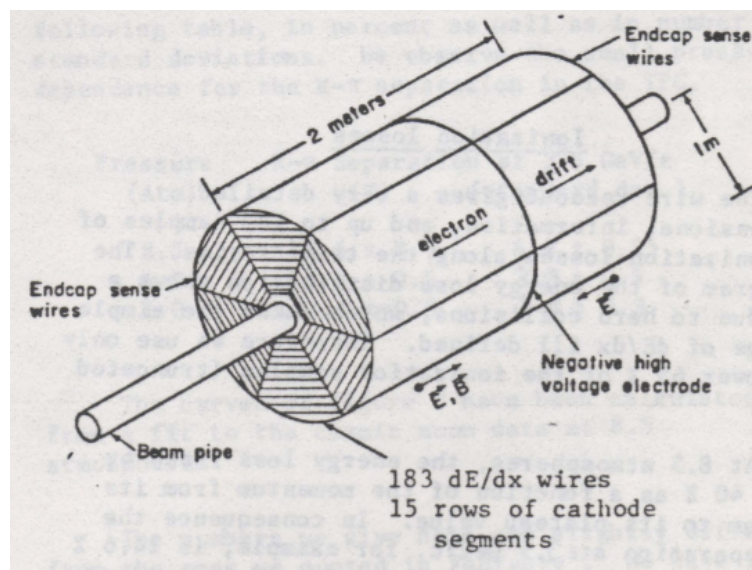
FIGURE 1.5: Schematic of the gas TPC used in the Positron Electron Project IV (PEP-4) experiment at the Stanford Linear Accelerator Center (SLAC).

Time-projection chambers (TPCs) come in two major variations: gas and liquid. Gas TPCs typically employ a chamber filled with an active gas medium inside a generated electric field with a position-sensitive electron collection system. The chamber is divided in half lengthwise via a central high-voltage electrode disc, and the disc establishes an electric field directed outward towards either end plate that is sometimes joined by a parallel magnetic field to minimize the outward diffusion of ionization electrons. As a particle propagates through the chamber, it ionizes the gas along its track, and the ionized electrons are drifted via electric field to a wire grid that provides positional information on their trajectory. The particle's Z-axis position is calculated using the electron's known drift time from the ionization event to the wire grid at the end, and a 3D representation of the particle track can then be reconstructed. The first example of a Gas TPC was the PEP-4 experiment at SLAC-PEP, which initially studied electron-positron collisions and particle identification by measuring the ionization losses in the relativistic rise

region[27]. Liquid TPCs generally function using the same principles as gas TPCs except with a liquid as the active medium. The most prominent form of liquid TPC used in modern neutrino experiments is the liquid argon TPC (LArTPC), which I discuss in depth in the next section.

1.3 Liquid Argon TPC

LArTPCs are designed to characterize long and short-distance neutrino oscillations by studying neutrino-nucleus interactions via fine-grained tracking, precise calorimetry, and particle identification capabilities. Charged particles ionize the liquid argon as they pass through the detector leaving a trail of ionized electrons in their wake. These ionization electrons are subject to an electric field that drifts them to sensing wires arranged in parallel planes along one side of the active volume. The wires within each plane are parallel to their neighbors and oriented at an angle to those in the adjacent planes as indicated in Figure 1.6[28]. The ionization charge is collected on the sensing wires, which are read out by the detector electronics. A three dimensional image of the readout can be reconstructed using the drift speed resulting from the electric field strength, the temporal data of the particle interactions, and the magnitude and duration of the charge signal. Both deposited charge and topology of the ionization are used for particle identification and calorimetry. In addition to the ionization that is created when charged particles travel through the argon, scintillation light is also produced, with a narrow spectrum peaked at 128 nm. The timing profile of this light has components which are understood via the decay of excimer states created during the interaction. The nature of these timing profiles depends on the presence of an electric field and on the level of impurities in the argon. Given the vacuum
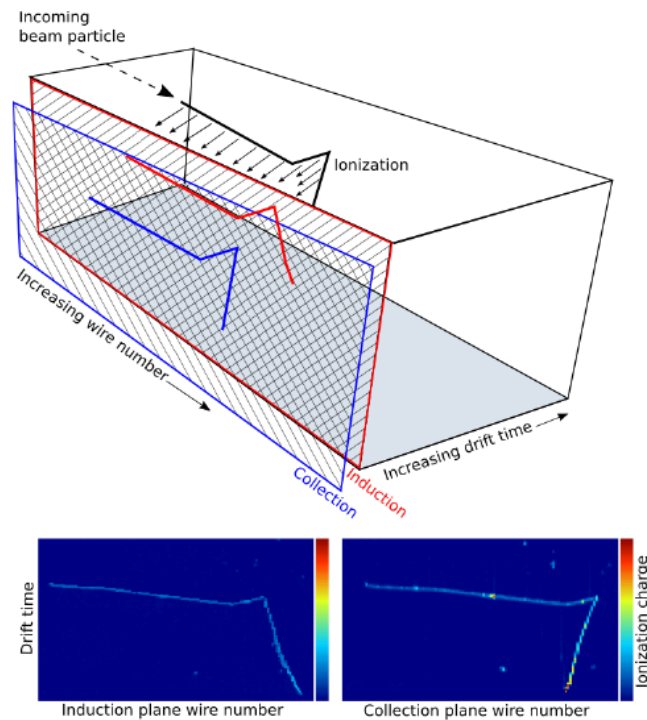
FIGURE 1.6: Schematic of the readout of a LArTPC caused by
a charged particle traversing the medium creating ionization
charge which is detected by sensitive wire planes containing
parallel wires typically spaced a few millimeters apart. Each
wire plane has its parallel wires oriented at a different angle rel-
ative to the adjacent plane, providing multiple 2D stereo-views
of the path of the ionization charge and the magnitude of the
deposited charge at each wire.

ultraviolet (VUV) nature of the scintillation light, traditionally a wavelength-
shifting material is used to enable detection by traditional light detection de-
vices (e.g., photomultiplier tubes or silicon photomultipliers) to detect them.
The prompt scintillation light signal (relative to the slow drifting ionization
signal) can be used as a trigger, indicating activity inside the LArTPC. This
light can also, as explored by the LArIAT collaboration, allow for an enhance-
ment in the calorimetric information provided by these detectors.

The LArTPC detector technology was pioneered by the ICARUS[29] col-
laboration, which also demonstrated the feasibility of using LArTPCs in long
baseline underground neutrino experiments through its run at the INFN

Gran Sasso Laboratory[30]. Following this effort, the Argon Neutrino Test-stand (ArgoNeuT) experiment[31] was deployed in the Neutrinos from the Main Injector (NuMI) beamline at the Fermi National Accelerator Laboratory (FNAL)[32]. The ArgoNeuT collaboration has published some of the first neutrino-argon cross section measurements[33–38], along with a number of calibration and detector studies[39, 40], serving as the start of the US-LArTPC program.

In 2012, LArTPC technology was chosen to follow up on the LSND/Mini-BooNE electron neutrino (ν_e) appearance anomaly[41, 42], since LArTPCs, unlike Cherenkov detectors, have the ability to distinguish between electron- and photon-initiated showers. The first phase of this follow-on experiment was the deployment of the Micro-Booster Neutrino Experiment (MicroBooNE) whose aim is to determine the true nature of the electron-like excess seen at low energies in MiniBooNE. The MicroBooNE detector[43] is an 89-ton active mass LArTPC located 470 m downstream of the Booster Neutrino Beam (BNB) target, just upstream of the MiniBooNE experiment. MicroBooNE serves as the pioneer LArTPC experiment on the BNB; the e/γ discrimination capabilities that are inherent to LArTPCs will allow MicroBooNE to determine the nature of the LSND/MiniBooNE anomaly. The second phase of this program, known as the Short-Baseline Neutrino (SBN) Program, will see the addition of two more functionally identical LArTPCs located on-axis in the BNB. The Short-Baseline Near Detector (SBND) will be a new 112-ton LArTPC serving as the near detector to the SBN program, located 110 m downstream of the BNB target. SBND will measure the unoscillated neutrino flux in the BNB, enabling searches in both the neutrino appearance and dis-appearance channels. The ICARUS-T600 detector, previously installed and operated at the Gran Sasso National Laboratory, now upgraded and shipped to FNAL, will serve as the far detector, located in a new building 600 meters from the BNB target. The large detector mass of ICARUS provides the

SBN program with the experimental sensitivity to definitively determine the nature of the ν_e appearance anomaly.

Further down the road, the Deep Underground Neutrino Experiment (DUNE)[44–47] aims to measure the CP phase in the neutrino sector and to determine the neutrino mass hierarchy using four massive LArTPCs totaling 40 kilotons fiducial mass. DUNE is positioned to be the world's flagship neutrino experiment for the next twenty years; it will use a high-power wide-band beam capable of producing neutrinos and anti-neutrinos directed from FNAL toward its underground LArTPCs located in the Sanford Underground Research Facility (SURF) 1300 km away in Lead, South Dakota. By measuring the asymmetry between appearance of electron neutrinos from a beam of muon neutrinos ($P(\nu_\mu \rightarrow \nu_e)$) compared to the appearance of electron antineutrinos from a beam of muon antineutrinos ($P(\bar{\nu}_\mu \rightarrow \bar{\nu}_e)$) as well as the precise measurement of the ν_e energy spectrum measured at the far detector, a measurement of both the CP violating phase and the ordering of the neutrino mass states, known as the mass hierarchy, can be done in the same experiment.

In this experimental landscape, the calibration and characterization of LArTPC response serves as a critical step in understanding the output of these detectors. This is where the Liquid Argon in a Testbeam (LArIAT) experiment enters[28].

In the subsequent chapters, the scientific goals of the LArIAT experiment will be outlined as well as the details of the experimental programs that were executed by the LArIAT collaboration between 2014 and 2017. Following this, the details of the experimental setup will be presented, including the LArIAT beamline instrumentation, the LArTPC, and its cold electronics and light detection devices, and then the details of the LArIAT software and data will be explained. Next, we will discuss Multiple Coulomb scattering and

how it applies to the LArIAT experiment, our techniques and scattering measurements, and how our results compare to previous results and scientific standards. We will finish with possible conclusions to be drawn from the experimental results and possibilities for future experiments.

Chapter 2

Liquid Argon In A Testbeam

The Liquid Argon In A Testbeam (LArIAT) experiment[28] is a type of liquid argon time projection chamber (LArTPC) designed to optimize calibration of LArTPC detector response for future and ongoing neutrino experiments. In Section 2.1, the purposes of the LArIAT experiment are described. In Section 2.2, the experimental setup is detailed including specifics about the charged particle beamline, time projection chamber (TPC), and the hardware work I did to support the experiment. Lastly, in Section 2.3, the software and data used in conjunction with LArIAT will be explained.

2.1   Purpose of LArIAT

A major contribution to systematic uncertainties in neutrino oscillation measurements comes from hadron-nucleon interaction cross sections and from the impacts of final state interaction (FSI) modeling[48] . This uncertainty enters both within the target nucleus and in how the hadrons emerge from the neutrino interaction and their ability to be detected.

Calibration of the LArTPC detector response for particles found emerging from neutrino interactions in the energy range relevant for the short-baseline and long-baseline neutrino experiments is one of the primary science goals of the LArIAT experiment. The design of the LArIAT LArTPC detector was

primarily driven to reproduce as closely as possible the technical features of larger future neutrino detectors based on this technology.

The LArIAT experiment, as described further in Section 2.2.2, has collected data with three different sets of wire planes with 3 mm, 4 mm, and 5 mm wire-to-wire spacing to allow for characterization of the e/γ separation power for multiple experimental setups.

The LArIAT experimental setup was designed to enable full exploration of the particle identification capabilities of the LArTPC technology. Auxiliary detectors in the charged particle beam tag particle species and incident momenta (or kinetic energy), providing the information that is necessary to check the performance of existing particle identification (PID) algorithms and further the development of such techniques.

Because current LArIAT PID algorithms significantly depend upon the tracking capabilities of the LArTPC, it is important to understand precisely how particles behave as they interact in the detector medium. The LArIAT LArTPC is in a unique position to study interactions of κ, π, μ, and p particles among others in a momentum range from 0.2-1.4 GeV/c. The magnet controlling the beam polarity is also configurable, thus providing the ability to select for positive or negative particles.

2.2   Experimental Setup

In this section a description of the charged particle beamline and associated non-LArTPC detectors is given. These detectors allow for the identification of the particle type entering the LArTPC at the heart of the LArIAT experiment. Moreover, the beamline detectors allow for precise incoming momentum to be measured, allowing for identification and characterization as a function of incident momentum.

2.2.1 Beamline

The Fermilab Test Beam Facility (FTBF) receives a 120 GeV/c primary proton beam with variable intensity, split by electrostatic septa from beam circulating in the Main Injector. Each supercycle of the Fermilab accelerator complex, roughly 60 seconds in duration, includes a four-second "spill" of primary beam to FTBF. Primary beam is sent to either or both of two experimental halls, named Meson Test and Meson Center.

The LArIAT experiment utilized the Meson Center beam line and had this primary beam focused onto a tungsten target. The resulting secondary charged particle beam is selected to have peak momentum between 8-80 GeV/c and is transported to the LArIAT experimental hall, designated MC7, where it is focused onto a copper target. This target, and the steel collimator hosting it, form the beginning of the tertiary particle beam and the LArIAT apparatus shown in Figure 2.1[28]. For most of the LArIAT data taking this secondary beam peak momentum was fixed at 64 GeV/c, although some lower secondary beam momentum settings were explored. The copper target produces a tertiary beam as a result of the energy of the secondary beam, which is comprised of mostly pions and protons, with a small fraction of electrons, muons, and kaons present as well.

The tertiary beam consists of a target and collimator system and two bending magnets. A set of four wire chambers and two time-of-flight scintillating paddles shown in Figure 2.1[28] provide tracking, momentum determination, and particle identification (PID).

The geometry of the tertiary beam line in MC7 has been optimized for LArIAT. A 13° production angle at the target, the target's enclosing collimator, and a 10° bend through a pair of dipole magnets provide particle momenta spectra tunable in the range from 0.2 to 2.0 GeV/c as a function of the field intensity in the magnets.
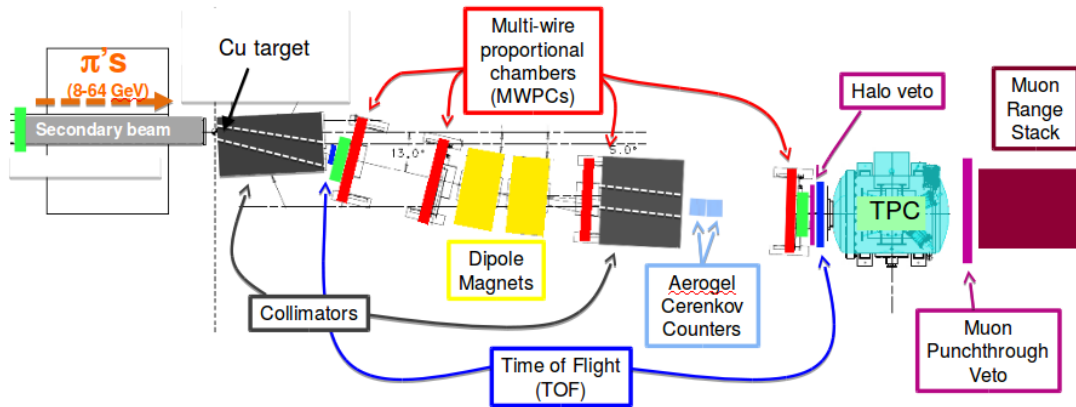
FIGURE 2.1: The tertiary beam line layout. Upstream and downstream collimators are in gray, bending magnets in yellow, wire chambers are in red, and the liquid argon TPC volume in green.

In the subsequent paragraphs, we will detail the various subsystems installed along the beamline.

The LArIAT time-of-flight (TOF) detector system consists of two scintillator paddles, which bracket the beamline and are shown in blue in Figure 2.1[28]. The upstream paddle has a small active area (10 cm x 6 cm) and was chosen to be a thin piece of scintillator to minimize any impact on the momentum of the particles coming from the target. Light guides were mounted on all four edges which lead to two PMTs mounted on the beam left side. The downstream paddle was chosen to have a slightly larger area (14 cm x 14 cm) and had two PMTs which were read out on opposite ends of the paddle. To improve performance and timing resolution in Run-III, the large area scintillator paddle was replaced with a smaller paddle similar to the upstream, and was read out with four new PMTs inherited from the muon g-2 experiment (E821 at BNL[49]) located on the diagonals of the counter.

The pair of spectrometer magnets in the LArIAT tertiary beam provide the necessary bend in the particle trajectory to allow for a momentum measurement. The aperture presented by the magnets is larger than that of the wire chambers; thus, only the central part of the magnet is utilized where

there is negligible variation of the field. The field intensity in one of the pair of magnets was measured using two Hall probes, both calibrated with NMR, to obtain the excitation curve shown in Figure 2.2[28]. The second magnet, having been made to the same standard and having the same history, is assumed to have a very similar response.
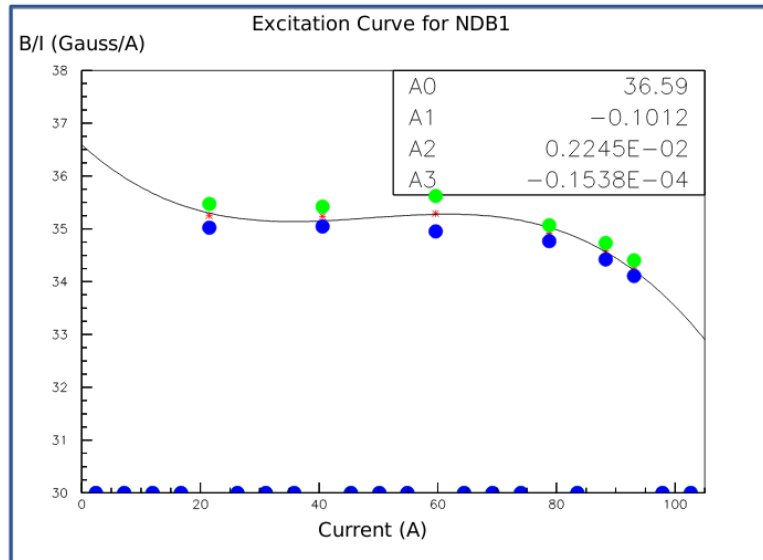
FIGURE 2.2: Excitation Curve, B/I vs. I, for one NDB magnet, using two Hall probes (blue and green). Parameters from a cubic fit (black curve) to average of measurements (red) given in legend.

The wire chambers are based on the Fenker Chambers[50] long in use at Fermilab. The chambers have been upgraded by adding additional grounding to improve the signal to noise in the electronic readout. The chambers, shown in Figure 2.3[28], have an effective aperture of 128 mm in both horizontal and vertical distances. The wires are spaced at 1 mm, with 128 wires in each view. The gas used is 85% Argon + 15% isobutane. The wire chambers typically operate between 2400 and 2500 volts. In a test beam, the chambers have typical efficiencies of 98% to 99% for protons at 120 GeV.

The aerogel threshold Cherenkov detector in the LArIAT beam line functions to separate muons and pions in the momentum range where muons emit Cherenkov radiation while pions do not. Aerogel is a material in which
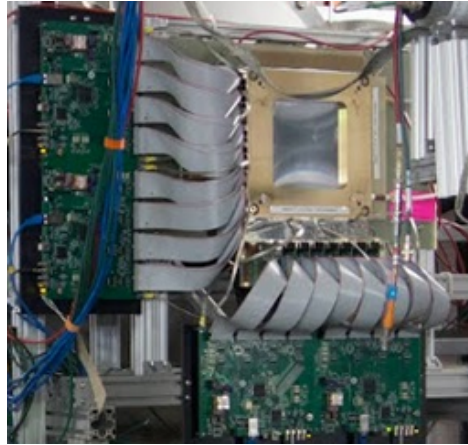
FIGURE 2.3: Image of one of the wire chambers used in the LArIAT tertiary beamline.

99.8% of the liquid component of the gel has been replaced with a gas. The result is a solid with extremely low density, low thermal conductivity, and low index of refraction. This technique was demonstrated by the MICE and Belle II experiments[51, 52]. LArIAT uses two aerogel threshold Cherenkov detectors with indices of refraction of 1.057 and 1.103. Having different indices of aerogel allows LArIAT to do separation in two different momentum ranges of interest. The Aerogel Threshold Cherenkov Detector with the refractive index of 1.103 is placed just behind the second collimator on the tertiary beam line, between the two downstream wire chambers. The aerogel detector was not used in this analysis.

The identification of particle tracks passing through the active volume of the TPC is augmented by placing calorimeters behind it to track the depth exiting particles penetrate into this material. Two detectors have been placed downstream of the LArIAT TPC: the punch-through detector and the muon range stack. These detectors were designed to play a role as a part of a trigger/veto system and in particle species identification and energy reconstruction.

The punch-through detector is composed of four identical scintillator slabs, optically coupled through tapering light guides to PMTs. These bars overlap, creating a rhomboidal region, where a passing particle encounters at least

two layers of scintillator. Signals from the PMTs are sent to a discriminator
and coincidence units. The resulting logic signal can be used as a part of all
trigger configurations used for taking beam data.

The muon range stack is the last detector in the LArIAT beamline, and
is used for the detection of beam particles that are energetic enough to pen-
etrate all the way through the TPC (and cryostat vessel). Its construction,
a simplified sampling calorimeter design consisting of eleven steel slabs of
various thickness and several layers of scintillator paddles, allows for more
detailed energy measurement of through-going particles.
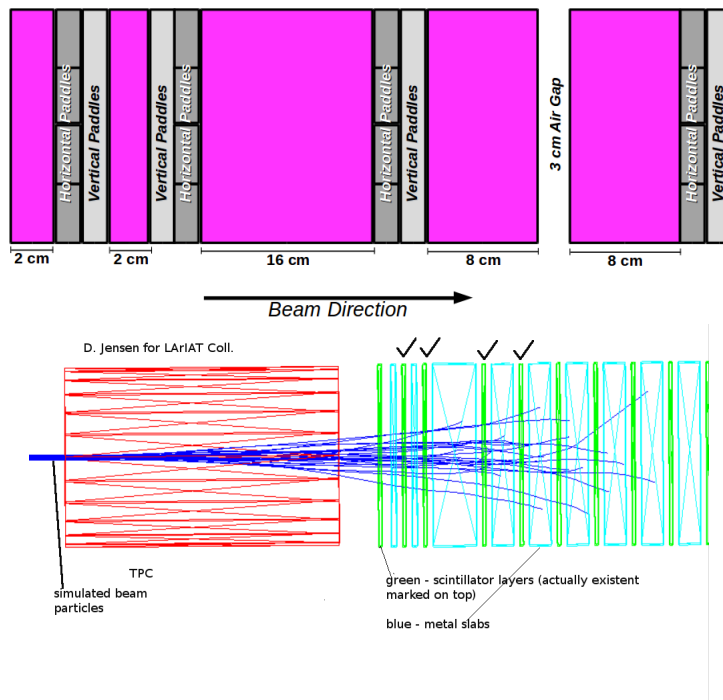
FIGURE 2.4: (Top) Schematic of the first five layers of the muon
range stack showing the orientation and relative position of the
scintillator paddles (grey) placed between the steel (pink). (Bot-
tom) Simulated muons passing through the LArIAT TPC (red
rectangle on the left) into the muon range stack (Green rectan-
gles on the right). Layers of scintillator existing in the actual
design are marked on the top of the picture (right part).

LArIAT's system to trigger on cosmic rays is based on two so-called "cos-
mic towers" which stand upstream and downstream of the cryostat—one
on beam right and one on beam left, framing the cryostat as seen in Figure

2.5 [28]. Each cosmic tower is composed of two paddle assemblies, upper and lower. The paddle assemblies each consist of four paddles, a matched pair which stand upright and a second matched pair lying across the top of the assembly, to act as a veto for downward-going cosmic ray air showers. Unless vetoed by the horizontal paddles, signals from paddle assemblies along the body diagonals of the TPC are combined in a logical "AND" to select cosmic muons crossing the TPC along one of its diagonals. A high proportion of events triggered this way contain cosmic ray tracks crossing both anode and cathode. Such tracks provide a sample of liquid argon ionization with effectively uniform linear ionization density, but they experience the entire range of charge attenuation available in the TPC before they drift to the anode. These tracks are used to calculate and monitor the level of electronegative contaminants in the liquid argon and provide a calibration sample for calorimetry and electric field studies.
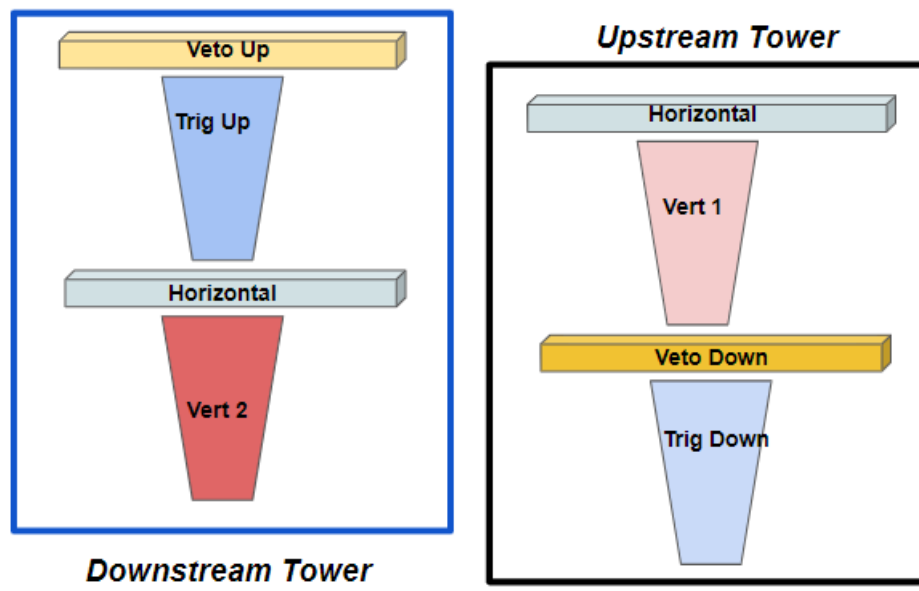
FIGURE 2.5: Schematic of the downstream and upstream cosmic detector paddle assemblies

2.2.2 TPC

The Liquid Argon Time Projection Chamber (LArTPC) can be broken down into three major subcomponents: 1) The high voltage system which provides the drift field voltage; 2) the cathode and field cage which steps down the high voltage through a network of voltage-dividing resistors to form a uniform electric field for charges to drift within; and 3) the wire planes which provide the charge sensitive readout for the detector. Here we describe each of the subcomponents which make up the LArIAT LArTPC.

The drift high voltage system for the LArIAT detector, shown pictorially in Figure 2.6[28], is designed to allow ionization electrons from the interaction of charged particles in the liquid argon to drift to the wireplanes. The high voltage system consists of a power supply capable of generating -125 kV and 16 mA of current. The voltage from the power supply is transmitted through high voltage cables to a series of filter pots before finally reaching the high-voltage feedthrough on the top of the LArIAT cryostat. This feedthrough brings the voltage into the liquid argon volume to be transmitted to the TPC cathode.
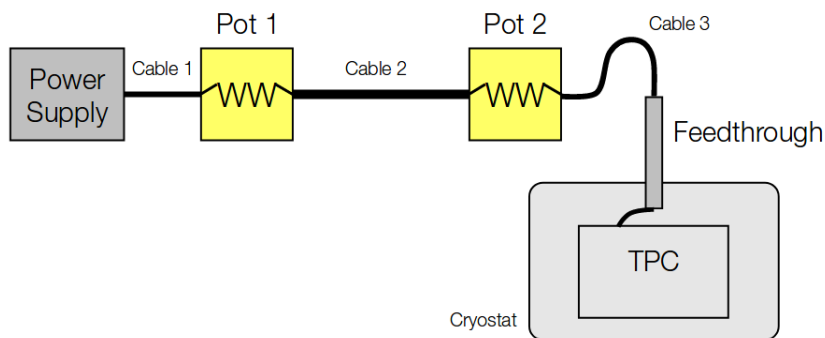
FIGURE 2.6: Schematic of the LArIAT high voltage system.

The dimensions of the TPC active volume are $47 \times 40 \times 90$ cm^3 (w $\times$ h $\times$ l), which is defined by the volume enclosed by the cathode and field cage structures. The rectangular field cage structure of the TPC is composed of

copper-clad G10[1] pieces, where the copper strips spaced at 1 cm intervals lining the TPC. The four walls of the field cage are connected electrically such that each copper strip forms a complete loop around the drift volume. Four 1 GΩ resistors are arranged in parallel between the strips of the field cage, for an effective strip-to-strip resistance of 250 MΩ. The circuit steps the voltage down in magnitude uniformly going from the cathode towards the anode, providing the uniform 500 V/cm electric field throughout the TPC active volume. EPCOS A71-H45X gas discharge tubes were used for surge protection, building on experience gained during MicroBooNE construction[53]. The cathode for the initial run of LArIAT was composed of a single piece of copper-clad G10 with the copper area of 40×90 cm^2 exactly matching the aperture of the field cage structure. The HV feed-through is electrically connected to the cathode using a simple flexible cable.

Before run III, the original cathode was replaced with a version composed of stainless steel frames able to hold a layer of steel mesh. This design served to test the behavior of wavelength-shifter foils installed on the cathode. During run IIIa the frames held one layer of mesh, resulting in a semi-transparent cathode, while during run IIIb TPB-evaporated foils were placed between two layers of mesh. Placing the di-electric foils behind the metal mesh served to avoid build up of positive ions drifting towards the cathode.

As shown in Figure 2.7[28], the LArIAT TPC has three drift volumes, each of which has its own electric field. The main drift volume is defined as the region between the cathode plane and the shield plane (C-S). Note that the shield plane wires are *not* read out. The other two drift regions are those between the shield plane and the induction plane (S-I), and between the induction plane and the collection plane (I-C). The electric field in these regions is chosen to satisfy the charge transparency condition to allow for 100% transmission of the drifting electrons through the shield and then the induction

---

[1]High-pressure curated fiberglass laminate.

planes.
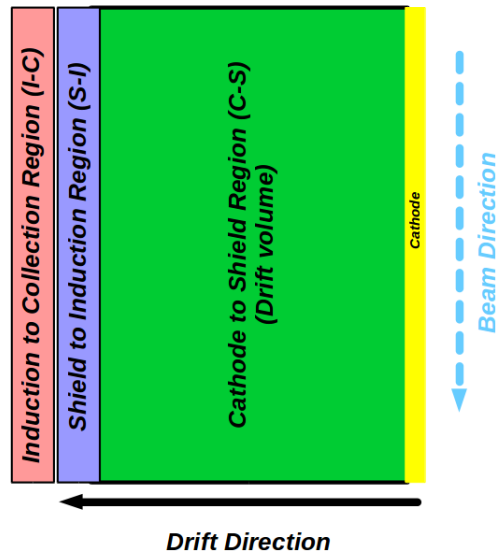
FIGURE 2.7: Schematic of the three drift regions inside the LAr-
IAT TPC: the main drift volume between the cathode and the
shield plane (C-S) in green, the region between the shield plane
and the induction plane (S-I) in purple, and the region between
the induction plane and the collection plane (I-C) in pink.

Once the wire planes have been wound and attached to their G10 boards,
the wires are soldered to their pads. Figure 2.8[28] shows the process of sol-
dering the wires in a photo taken by the author. Once all wires have been
soldered in place, the wires are broken off behind the solder pads and the
temporary epoxy strip is removed. The entire board is cleaned with ethyl
alcohol to remove any residue of solder flux before the finished wire planes
ahead of installation in the TPC.

2.2.3 Cryogenics

The LArIAT cryostat, shown in Figure 2.9[28], was repurposed from the Ar-
goNeuT experiment with a series of modifications to allow for operations in a
charged particle test beam. The cryostat consists of an inner volume contain-
ing the purified liquid argon and an outer volume serving as a vacuum jacket
with layers of aluminized mylar. The main axis of the cryostat is horizontal
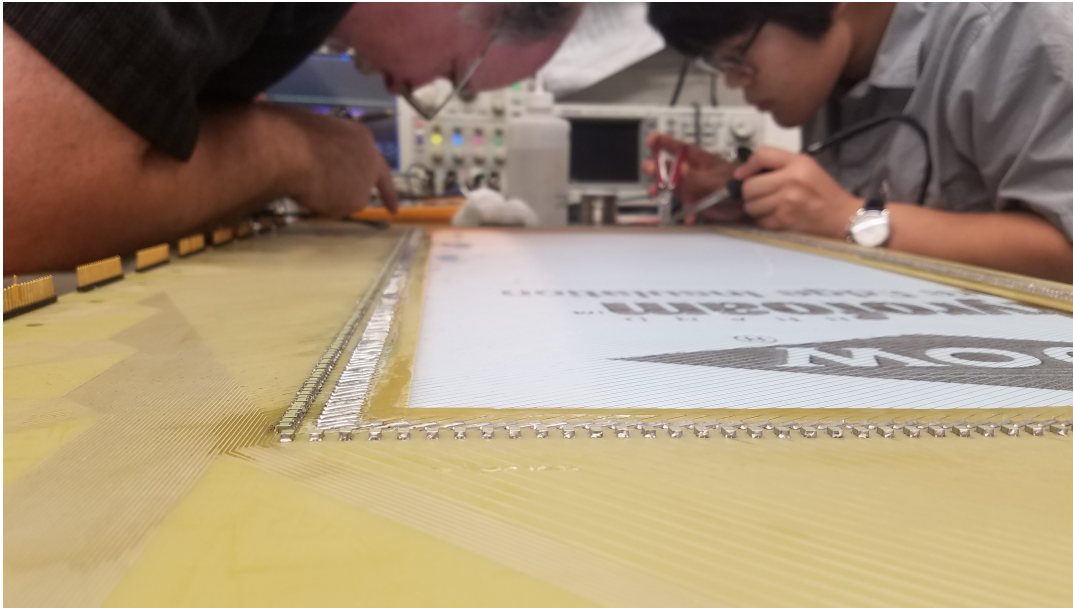
FIGURE 2.8: Author's photo of the wire plane soldering process
during troubleshooting between Run-II and Run-III.

and oriented parallel to the beam. The inner vessel is 76.2 cm in diameter and
130 cm in length, corresponding to a liquid argon volume of about 550 L, or a
mass of 0.76 t. The cryostat has a wide neck, or "chimney", protruding from
its top at mid-length which serves as an access path for signal cables from
the LArTPC and the internal instrumentation, as well as for the high voltage
feedthrough.
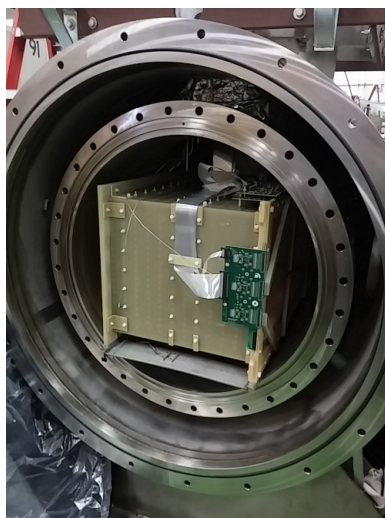
FIGURE 2.9: The LArIAT cryostat open with the TPC placed in
the inner volume.

LArIAT uses liquid argon with a specified maximum contamination of 2 parts per million (ppm) oxygen, 3.5 ppm water, and 10 ppm nitrogen. Free electrons readily attach to oxygen and water molecules as they drift through the detector volume, so they must be avoided. Nitrogen contamination is detrimental to the collection of scintillation light. The level of these contaminants in the delivered argon is determined using a suite of commercial gas analyzers.

The argon is delivered from the commercial dewar to the cryostat through 2.54 cm diameter schedule 10 stainless steel piping insulated with 20.32 cm of polyurethane foam. The argon then passes through LArIAT's argon filtration system. The purification system consists of a single 77 liter filter which is filled halfway with a 4A molecular sieve that primarily removes water contamination but can also remove small amounts of nitrogen and oxygen. The remaining volume of the filter contains BASF CU-0226 S, a highly dispersed copper oxide impregnated on a high surface area alumina, to remove oxygen and water. The filter is insulated with a vacuum jacket and aluminum radiation shields, and the filter media are regenerated in place using heated gas. The filter media are very efficient at removing oxygen and water and the argon is pure enough after a single pass through the media to allow several millisecond electron drift lifetimes in the TPC.

From the filter, the argon is directed into the inner cryostat via a liquid feedthrough on the top of the cryostat. The feedthrough continues down into the inner volume via a pipe the deposits the incoming liquid into the bottom of the cryostat volume. The argon level, temperatures, and pressures are continuously monitored during operation both in the commercial dewar supplying the argon as well as the levels inside the cryostat, as shown on the top of Figure 2.10[28]. The argon in the cryostat is allowed to boil and vent to the atmosphere during operation and the argon level is monitored via the level probes. Flow of argon into the cryostat is enabled whenever the liquid

level goes below a predetermined value to ensure that the TPC high voltage feedthrough and cold electronics are always submerged. During normal operations, the liquid level inside the cryostat is replenished several times per day, as can be seen by the cycle of the liquid level and valve positions shown at the bottom of Figure 2.10[28].

The temperature of the argon inside the cryostat can be determined through direct use of temperature probes based on Resistance Temperature Detectors (RTDs) deployed at the bottom, middle, and top of the cryostat (listed as TE213A, TE314A, and TE212A in Figure 2.10[28] respectively). This can be crossed check using the pressure in the cryostat gas volume and extrapolating this to the center of the liquid volume. The pressure at the surface of the liquid argon is maintained by the cryo-system at $\sim$20 psi $\pm$.0.4 psi.

We also measure the pressure in the cryostat gas volume and calculate the pressure at the center of the TPC to cross-check the temperature inside the TPC. From this pressure and the boiling point curve of argon, we calculate the temperature.

2.2.4 Electronics

The LArIAT TPC front-end electronics comprises a 480-channel analog signal path from the TPC wireplanes to the signal digitizers. The front-end system also includes a digital control system for the TPC-mounted electronics, a power supply, and a distribution system. A block diagram of the overall system is shown in Figure 2.11[28].

The electrical signals on the TPC readout wires are typically quite small, being a direct readout of the ionization of the liquid argon. To achieve a good Signal-to-Noise Ratio (SNR) for such signals, the LArIAT TPC is instrumented with cold amplifiers developed by Brookhaven National Lab (BNL) and mounted directly to the TPC frame inside the liquid argon cryostat. The

BNL amplifiers are built as custom Application-Specific Integrated Circuits (ASICs). The BNL ASICs adopted in LAriAT are designated as LArASIC.

2.3 Software and Data

The beamline and TPC data used in this analysis was simulated, reconstructed, and analyzed with version 6.34.01 of the Liquid Argon Software (LArSoft) framework. LArSoft provides an integrated, art-based, experiment-agnostic set of software tools for all planned and running LAr neutrino experiments at Fermilab to perform simulation, reconstruction and analysis. LArSoft uses C++ and is built on the ROOT data analysis software and the *art* analysis framework supported by the Fermilab Scientific Computing Division for intensity frontier experiments. The software framework is compatible with git / mrb / ups, and the core LArSoft code includes detector interfaces, simulation and reconstruction data structures, event data reconstruction algorithms, data simulation algorithms, and plug-in interfaces.

The reconstruction process begins with the digital information received from the wire plans within the TPC. Its goal is to use these basic digital signals to identify the particles in an interaction event in the detector via a fully reconstructed 3D visualization of the particle tracks. The basic steps, which will be outlined further in Section 4.3, move consecutively through raw data reception, signal processing, hit-finding, clustering, shower-finding, flash-finding, and analysis-phase reconstruction[54]

FIGURE 2.10: *(top)* Screenshot of the LArIAT cryosystem monitoring page showing the levels of the argon both inside the cryostat and in the supply dewar as well as the monitored levels plotted over a twenty-four hour period. *(bottom)* Plots showing the liquid argon level inside the cryostat as well as the corresponding liquid valve which allows argon to flow into the cryostat and the level drops due to boiling. The frequency of the typical fill/vent cycle can be seen with the typical time between fills being slightly more than 3 hours.

FIGURE 2.11: Overview of LArIAT Front End electronics.

Chapter 3

Multiple Coulomb Scattering

This chapter provides an overview multiple coulomb scattering (MCS) theory as applies to LArTPC's. Historical and current MCS experiments will then be explained, which will finally lead to an explanation of the goals and techniques used in this analysis.

3.1 General Overview

The propagation of a particle in a medium depends upon interactions of the particle with the medium itself. Particles often interact inelastically with atomic electrons and elastically in a process called multiple Coulomb scattering. MCS represents the multiple electromagnetic interactions between a charged particle and the atomic nuclei of the medium the particle traverses. When a particle experiences a single coulomb scatter in a medium with thickness on the order of 1 μm, the effect is well described by the Rutherford formula[55]

$$d\sigma/dcos\theta = \frac{\pi}{2}z^2Z^2\alpha^2\left[\frac{\hbar c}{KE}\right]^2\frac{1}{(1-cos\theta)^2} \tag{3.1}$$

where $d\sigma/dcos(\theta)$ is the differential cross section, θ is the scattering angle, Z is the atomic number of the medium, KE is the kinetic energy of the particle, and α is the fine-structure constant. As the number of interactions and thickness of the interaction medium increase, MCS results in a statistical angular

deviation of the charged particle from its original trajectory.

In the simple two-dimensional representation shown in Figure 3.1, we define the incident momentum as p_{inc}, the outgoing momentum as p_{out} and the scattering angle as θ_0. According to the theory of Molière[56], the scattering angle distribution is Gaussian-like at small angles ($\theta_0 < 10°$) with a more moderate Rutherford-like tail. It is customary to model the distribution of the scattering angles at a given incoming momentum for small angles with a Gaussian centered at zero and standard deviation σ_{MCS} given by the Highland-Lynch-Dahl formula (referred to as the Highland formula in what follows)[57].

The Highland formula reads

$$\sigma_{MCS} = \frac{S_2}{p_{inc}\beta c}z\sqrt{\frac{l}{X_0}}[1 + \epsilon \ln\left(\frac{l}{X_0}\right)], \qquad (3.2)$$

where c is the speed of light, β is the speed of the particle in units of c, z is the magnitude of the charge of the particle, l is the width of the material traversed, and X_0 is the radiation length in the medium. S_2 and ϵ are experimental parameters determined to be 13.6 MeV and 0.038 respectively[58] as discussed further in Section 3.2, and they will be reevaluated with respect to the LArIAT LArTPC in Section 3.3.

3.2 Previous Results

The accuracy of the Highland formula has historically been demonstrated on several occasions to be within the range of $\pm$ 5% as Highland originally claimed in 1975[59].

The experimental parameters S_2 and ϵ in the Highland formula 3.2 play a fundamental role in the accuracy of its predictions. S_2 and ϵ were originally determined to be 13.6 MeV and 0.036 respectively using a global fit
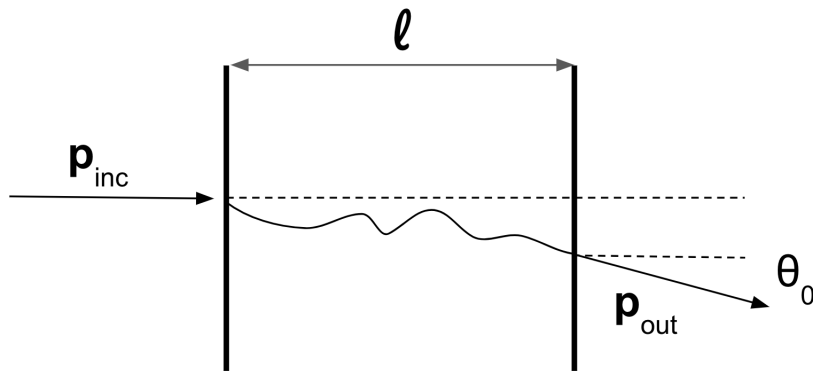
FIGURE 3.1: 2D sketch of multiple coulomb scattering event in a medium.

to MCS simulated data using a modified Geometry and Tracking (GEANT) simulation package of 14 different elements and 7 thickness ranges. All of the simulated particles were relativistic, with $\beta = 1$. The materials studied ranged from hydrogen (Z=1) to uranium (Z=92)[57].

In 1999, B. Gottschalk *et al*. measured multiple Coulomb scattering of 158.6 MeV protons in fourteen materials from beryllium to uranium including brass and several plastics. Targets ranged from thin (negligible energy loss) to very thick (greater than the mean proton range). The scattering angle distribution was measured by means of a single diode dosimeter scanned typically over two decades of dose falloff. Each data set was fitted with a Gaussian distribution to extract a characteristic angle θ_0. The θ_0 values were compared with the Highland formula using Gottschalk's own generalization to thick targets. The distribution of the deviation from Highland theory for 115 independent measurements was as expected, with a mean value of $-2.6 \pm 0.5\%$ and an rms spread of 6%[60].

With its demonstrated accuracy for some materials, particle types, and momentum ranges, the Highland formula can be employed as a tool for various circumstances where charged particle momentum calculation is problematic and scattering angle data is readily available. In 2017, MicroBooNE

utilized the Highland formula to determine muon momentum within their LArTPC because it did not require a full particle ionization track to be contained inside of the detector volume, unlike range-based momentum reconstruction and calorimetric momentum reconstruction[61].

However, given that the parameters S_2 and ϵ in the Highland formula were determined from a single fit to a wide range of particles and material thicknesses, MicroBooNE believed that they could differ for scattering specifically in liquid argon with $l \approx X_0$. They also had reason to believe that the
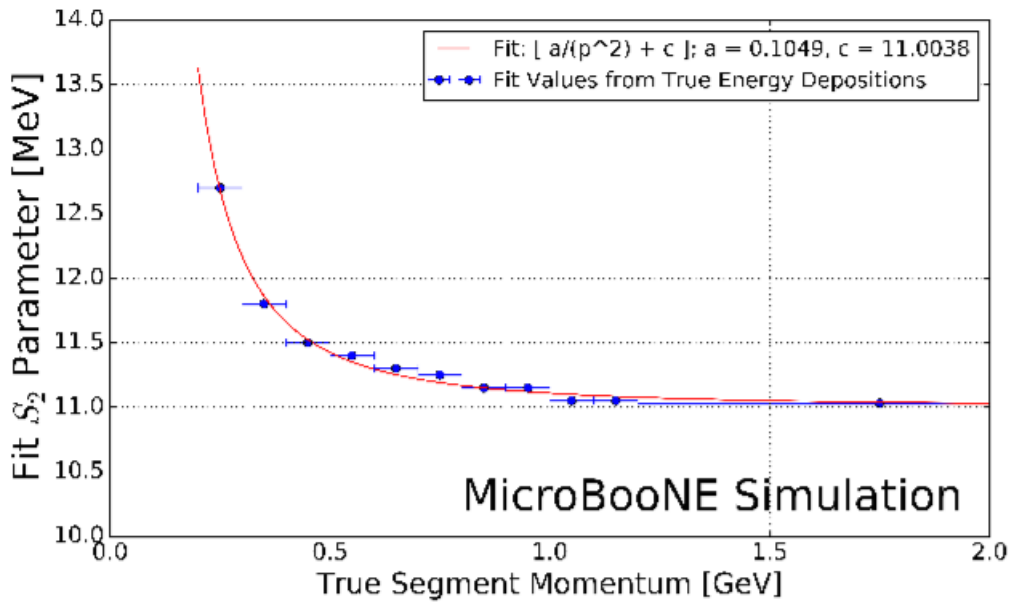
FIGURE 3.2: Fitted Highland parameter S_2 as a function of true segment momentum for $l = X_0$ simulated muons in the MicroBooNE LArTPC.

parameters might be momentum dependent for particles with $\beta < 1$. MicroBooNE tested their hypothesis by simulating a large sample of muons inside the MicroBooNE TPC using GEANT4 and simplifying the Highland formula by using track segments of length $l \approx X_0$ so that

$$\sigma_0^{HL} = \frac{S_2}{p\beta c}. \tag{3.3}$$

With the formula's dependence on ϵ now removed, they measured true energy depositions S_2 at several true track segment momenta and fit a plot of S_2 vs. true momentum with a modified momentum-dependent function

$$S_2 = a/p^2 + c \tag{3.4}$$

as seen in Figure 3.2 [61]. This functional form was chosen because it captures the trend in the fit value of S_2 with respect to momentum and asymptotically approaches a constant value when β approaches 1. The fitted value of S_2 was consistently less than the standard 13.6 MeV for momenta greater than 0.25 GeV/c, and the fit returned values of 0.105 MeV and 11.004 MeV for a and c respectively. The resulting Highland equation used in this study was thus

$$\sigma_0^{RMS} = \sqrt{(\frac{\kappa(p)}{p\beta c})^2 + (\sigma_0^{res})^2} \tag{3.5}$$

where $\kappa(p)$ is the newly modified function

$$\frac{0.105 MeV}{(p(GeV))^2} + 11.004 MeV \tag{3.6}$$

and σ_0^{res} is 3 mrad based on MicroBooNE simulation studies of muons at higher momenta. A visualization of the Highland prediction before and after tuning can be seen in Figure 5.2[61]. With the tuned formula, the Highland calculation and simulation data agreed for contained tracks, with a small bias in the momentum reconstruction and with resolutions that varied as a function of track length, improving from about 10% to 5% from shorter to longer tracks. For simulated exiting muons with at least one meter of track contained, there was a similarly small bias and a resolution less than 15% for muons with momentum below 2 GeV/c. On this basis, MicroBooNE asserted that the standard Highland formula should be re-tuned specifically for scattering in liquid argon[61].
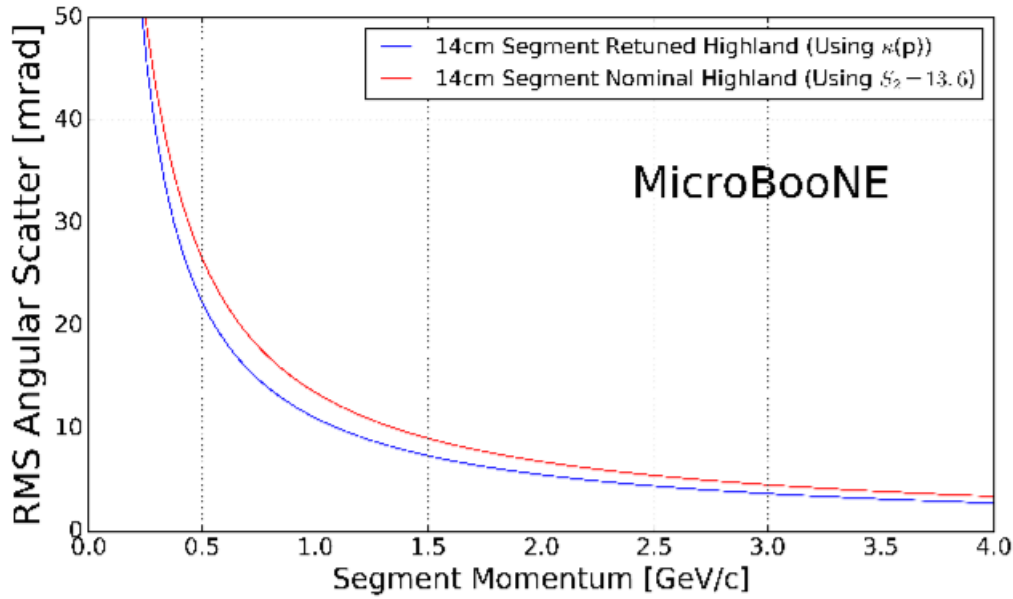
FIGURE 3.3: The Highland scattering σ_0^{HL} for 14 cm segment lengths and $\sigma_0^{res} = 0$ as a function of true momentum before and after tuning.

3.3 Our Technique

The technique used in this analysis is intended to tune the experimental constant S_2 of the Highland formula 3.2 to more accurately reconstruct the momenta of various particle types in liquid argon from their multiple Coulomb scattering angle. This technique diverges from that of the simplistic two-dimensional model explained in Section 3.1 and the techniques used in previous analyses due to our attention to three-dimensional scatters, our unique exponential fit approach to the standard deviation, and our reliance on a data-driven, particle-dependent constant value for S_2.

In a more realistic three-dimensional representation of multiple Coulomb scattering shown in Figure 3.4, we define θ_x and θ_y as the angle between the projections in the XZ and YZ planes. These angles are both distributed as gaussians centered at zero with standard deviation σ_x and σ_y respectively,
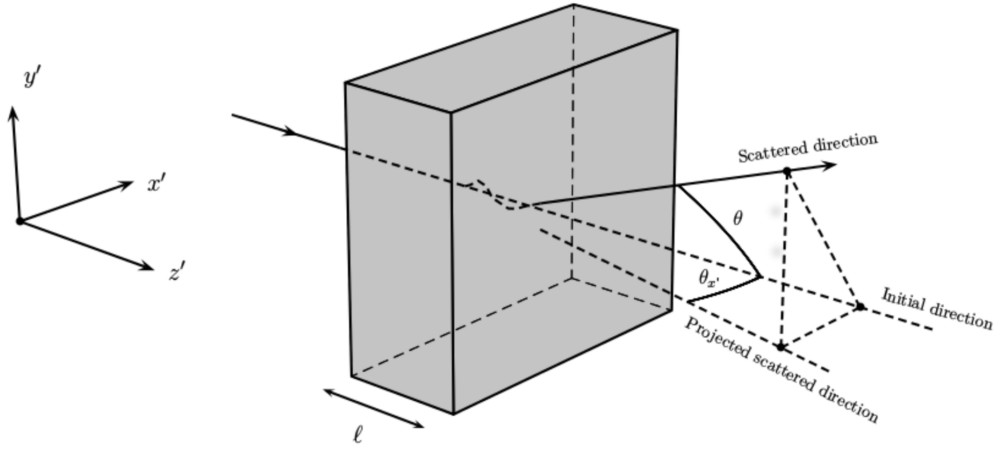
FIGURE 3.4: 3D sketch of a multiple coulomb scattering event in a medium.

mathematically expressed as

$$\theta_x \sim \mathcal{N}(0, \sigma_x^2) \text{ and } \theta_y \sim \mathcal{N}(0, \sigma_y^2). \tag{3.7}$$

For small angles, we can approximate the 3D angle between the incoming and outgoing momenta as

$$\theta_{3D}^2 = \theta_x^2 + \theta_y^2 \tag{3.8}$$

We can assume that θ_{3D}^2 is distributed as the sum of two independent gaussian distributions with the same mean $\mu_x = \mu_y = 0$ and same standard deviation $\sigma_x = \sigma_y = \sigma_0$ such that

$$\theta_{3D}^2 = \sum_{i=x,y} \theta_i^2 \sim \sum_{i=x,y} \Gamma(1/2, 2\sigma_i^2) = \Gamma(n/2, 2\sigma_0^2), \tag{3.9}$$

where n is the number of gaussian-distributed variables in the sum (in our case $n = 2$) and Γ is the gamma distribution. Substituting n, we simply find

$$\theta_{3D}^2 \sim \Gamma(1, 2\sigma_0^2). \tag{3.10}$$

A common analytical parametrization of the gamma distribution in the k and α parameters is as follows:

$$\Gamma(k,\alpha) = \frac{1}{\Gamma(k)\alpha^k}x^{k-1}e^{-\frac{x}{\alpha}}, \tag{3.11}$$

where $\Gamma(k)$ is the compact version of the factorial, $\Gamma(k) = (k-1)!$

In our case, the form of the gamma distribution is greatly simplified by the fact that $k = n/2 = 1$. In fact, $\Gamma(1) = 1$, $x^{k-1} = x^0 = 1$ and the gamma function becomes:

$$\theta_{3D}^2 \sim \Gamma(1, 2\sigma_0^2) = \frac{1}{2\sigma_0^2}e^{-\frac{\theta_{3D}^2}{2\sigma_0^2}}. \tag{3.12}$$

The form of the function used to fit the θ_{3D}^2 distributions is the following

$$\theta_{3D}^2 \sim Ce^{\alpha\theta_{3D}^2}, \tag{3.13}$$

where C is a normalization factor and $\alpha = -\frac{1}{2\sigma_0^2}$. Thus, accounting for the propagation of uncertainties, we find

$$\sigma_0 \pm \delta\sigma_0 = \sqrt{-\frac{1}{2\alpha}} \pm \sigma_0\frac{\delta\alpha}{2\alpha}, \tag{3.14}$$

where $\delta\alpha$ is the uncertainty of the fit parameter.

In order to calculate the Highland formula as a function of the momentum, we divide LArIAT data and Monte Carlo events into bins of incident momentum. For each bin, we plot the θ_{3D}^2 distribution, we fit it with an exponential curve, and we find the slope. Then we calculate $\sigma_0 \pm \delta\sigma_0$ from the estimated slope and the fit uncertainty as described above. With this technique, we have measured the Highland formula on LArIAT data events for κ^+ and π^+/μ^+ as well as Monte Carlo events for κ^+, π^+, μ^+, and protons.

Once this data was obtained, the standard Highland formula (using $S_2 = 13.6MeV$, $\epsilon = 0.038$, $\chi_0 = 14cm$ and $l \approx 14cm$)

$$\sigma_0^{HL} = \frac{13.6MeV}{p\beta c},$$ (3.15)

and the "tuned" Highland formula (using $\epsilon = 0.038$, $\chi_0 = 14cm$ and $l \approx 14cm$)

$$\sigma_0^{THL} = \frac{S_2^T}{p\beta c}$$ (3.16)

were plotted together for comparison. The Highland formula tuning process was done by fitting the energy depositions in each momentum bin of each available data particle type with the function $\sigma_0 = \frac{S_2^T}{p\beta c}$ with S_2^T being the fit parameter and σ_0 calculated from data. The results of these fits can be seen in Figure 3.5.

This new particle-dependent, data-driven constant S_2^T was then used in place of the S_2 constant in the Highland formula to create a variation of the Highland formula tuned specifically for each particle type in the LAr-IAT LArTPC. Highland calculations for Monte Carlo κ^+, μ^+, π^+, and proton events were then plotted on top of the nominal Highland formula and tuned Highland formula for each respective particle type. It is important to note that the S_2^T constant used in the tuned Highland formula for this comparison is the same S_2^T that was derived from data.
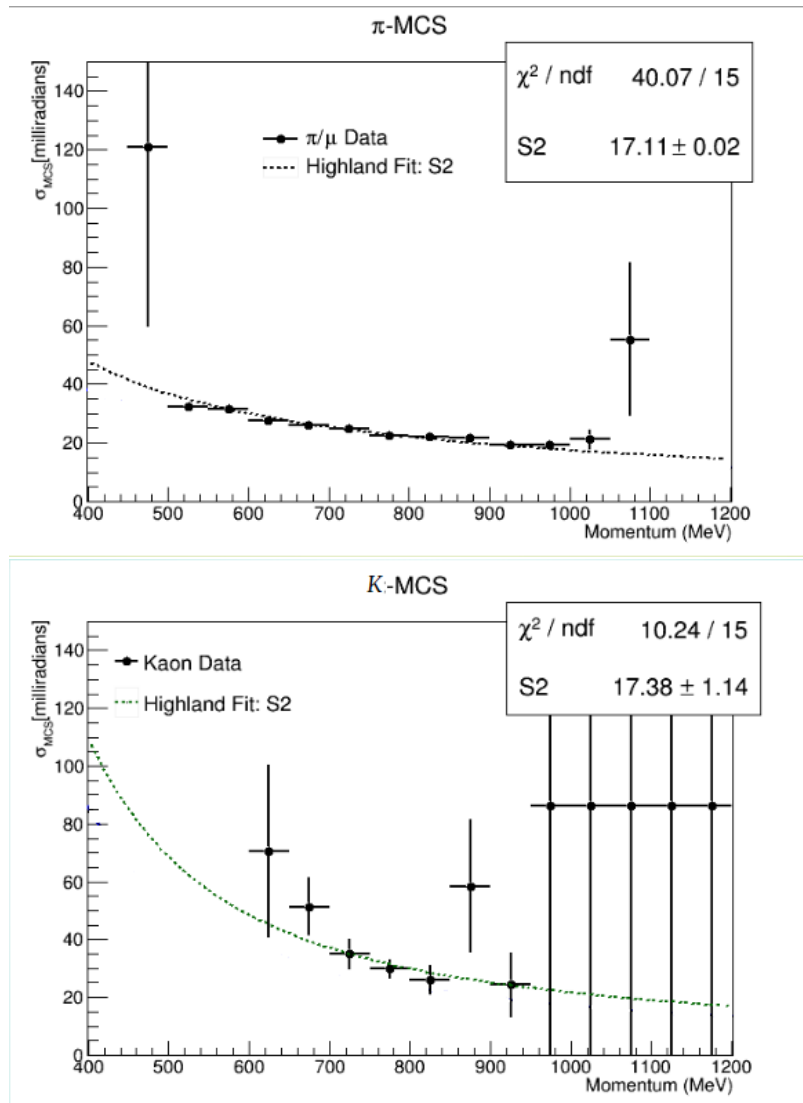
FIGURE 3.5: The plot of the fit S2 Parameter vs. particle track momentum per data particle. The left figure is the fit for data π^+/μ^+ particles, right is for data κ^+ particles.

Chapter 4

Measurement

In this chapter, the Highland measurement will be discussed including details about the data and Monte Carlo samples used, reconstruction techniques, and results for data and Monte Carlo measurements. The results will be displayed as a series of histograms for each particle type: first the one-dimensional histograms showing the distribution of scattering angles at various consecutive momentum ranges which are then extrapolated via the fitting process described in Section 3.3 to the second set of histograms showing the two-dimensional plot of momentum vs. standard deviation. The second set histograms are plotted on top of reference curves representing the nominal and tuned Highland formulas 3.15 and 3.16 respectively, and our various methods of comparison are later discussed in Chapter 5.

4.1 Data Samples

The pion and kaon data set used in this analysis come from a December 2017 "Picky" run in the LArIAT detector. The "Picky" parameter is used to optimize reconstruction for efficiency and low background. This tracking algorithm works by requiring that the wire chamber have exactly one unique hit in each wire plane. This requirement greatly increases the probability that each hit originated from the same incident particle to an uncertainty of about 1%. The kaon data set consists of 1081 events of K^+ particles with momenta

ranging from 500-1100 MeV/c. The pion/muon data set consists of 15,916 events of about 82% π^+ particles and about 18% μ^+ particles with momenta ranging from 450-1200 MeV/c. Some histograms in Section 4.4 have been omitted due to null data population.

4.2 Monte Carlo Samples

The Monte Carlo portion of this analysis consists of simulated π^+, p, K$^+$, and μ^+ particles with momenta ranging from 400-1200 MeV/c. We use a combination of the G4Beamline Monte Carlo [62] and the Data Driven single particle Monte Carlo (DDMC) to generate simulations of LArIAT events and dataset particle composition. G4Beamline Monte Carlo is used to simulate the particle transport in the LArIAT tertiary beamline and calculate the particle composition of the beam leading to the TPC. The DDMC uses the G4Beamline momentum and position data at wire chamber 4 to generate the event within the TPC. The π^+ sample contained 147,075 events from the 100A pion run-II positive polarity data-driven Monte Carlo beam configuration after relevant cuts and filters discussed in Section 4.3. The p sample contained 71,138 events from the 100A proton run-II positive polarity data-driven Monte Carlo beam configuration after relevant cuts and filters. The K$^+$ sample contained 172,502 events from the 100A kaon run-II positive polarity data-driven Monte Carlo beam configuration after relevant cuts and filters. The μ^+ sample contained 272,086 events from the 100A muon run-II positive polarity data-driven Monte Carlo beam configuration after relevant cuts and filters. Some histograms in Section 4.5 have a poor statistics due to a low data count or have been omitted entirely because of a null data count. These occurrences will be discussed further in Section 5.1.

4.3   Reconstruction Techniques

The first stage to successfully reconstructing Monte Carlo data is Generation, Simulation, and Digitization (GenSimDigi). The function of this stage is to generate a Monte Carlo momentum and θ distribution, simulate a response to these distributions in LAr, and then simulate the LArIAT electronics response to the simulated LAr response signals so that it looks similar to true data. Once similarity is achieved, the events move to the reconstruction stage for identification and measurement.

As outlined in Section 2.3, the job of reconstruction is to use unipolar pulses received from the induction and collection plane wires in both simulated Monte Carlo and in data to accurately identify particle data via their 3D track topology. The process begins with the raw wire data, represented by a waveform on a channel. The raw data is composed of an interaction signal, background noise, and a pedestal offset, and each of these must be processed to acquire the optimal signal-to-noise ratio. This optimization is done through a process called deconvolution. Once the data has been deconvoluted, the next step is hit-finding. Hit-finding groups together Analog to Digital Converter (ADC) signals from each wire to determine "hits". Hits correspond to physical ionizations within the TPC that occur as the particle traverses the LAr. Hit-finding thus provides the track start and end positions as well as some geometric information. Hits are then grouped together by time and space in a process called clustering, which allow us to organize them into 3D objects, tracks, or showers. A shower-finding algorithm is then employed to tag showers. This leads to the second phase of reconstruction, called the "Analysis-phase" reconstruction. Energy and dE/dx are estimated for each track, which lead to a momentum estimation and particle identification. The momentum of the scattering track has taken into account

the energy loss from Wire Chamber 4, where the initial momentum measurement is made, to the point inside the TPC where the incoming best fit line and outgoing best fit line intersect using the equation

$$P_{TPC} = \sqrt{P_{WC4}^2 + E_{LOSS}^2 - 2E_{LOSS}\sqrt{P_{WC4}^2 + m^2}} \tag{4.1}$$

with E_{LOSS} being the energy loss of each particle type through the various media leading up to the intersection point.

Once these processes have successfully defined a particle and its characteristics, we run our custom Highland Formula Module to analyze the particle track for the data we need. The first step of this analysis is called the Wire Chamber to TPC Match (WC2TPC), and is particularly useful in instances where more than one track is reconstructed either due to multiple interactions within the detector or due to pile up of other particles when the readout is triggered. WC2TPC matches one wire chamber track to one reconstructed track by measuring the angle α between the wire chamber trajectory and reconstructed trajectory, and the positional difference between the projected start point of the track inside the TPC from the wire chamber track and the actual reconstructed start point of the track inside the TPC. The latter value is measured as

$$\Delta R = \sqrt{\Delta x^2 + \Delta y^2}. \tag{4.2}$$

with δx and δy being the difference in position of the wire chamber trajectory and reconstructed trajectory for x and y respectively. If $\alpha < 8°$ and $\Delta R < 4$ cm, WC2TPC determines this to be a match, and any events with multiple matches for a single track are removed.

With this successfully matched track, we can apply our filters and cuts needed for the final process of finding the 3D angle between the incoming and outgoing track. In the first filtering process, we selected the first 28 cm of particle tracks 28 cm or longer after standard fiducial cuts. Fiducial cuts

serve to filter out portions of tracks in areas along the edges of the detector where the electric field is poorly characterized, leaving us with an effective TPC volume from 1 cm to 41.5 cm in the x direction, -19 cm to 19 cm in the y direction, and 1 cm to 89 cm in the z direction for the LArIAT LArTPC. By eliminating the pieces of tracks that are in these incompatible areas, we are left with tracks that behave as expected. We then split these tracks to make two 14 cm tracks intersecting at the middle, and calculate the 3D angle between their individual best-fit lines using standard Root functions. The tracks have been chosen to be 14 cm to simplify the Highland equation as discussed in Section 3.3. The Highland Formula module also provides us with values for total number of points in the track, number of spacepoints in the first track segment, number of spacepoints in the second track segment, χ^2/ndf for the full track, χ^2/ndf for the first track segment, χ^2/ndf for the second track segment, an estimate of the energy loss before the TPC front face, and the particle track momentum as measured at wire chamber 4.

4.4 Data Results

In Figures 4.1-4.4, the distribution of the square of the 3D angle is plotted for each momentum range of each particle. The distribution is fit with an exponential function as outlined in Section 3.3 with fit parameters and errors listed in the table of each histogram. In Figure 5.1, the MCS standard deviations are plotted against each momentum bin for each particle. The x-coordinate of each point is taken to be the center of each momentum bin, with the bin width being the x error. The y error is calculated using Equation 3.14. The nominal Highland formula curve is superimposed on each histogram for comparison, and the tuned Highland formula is fit to the data for each particle species.
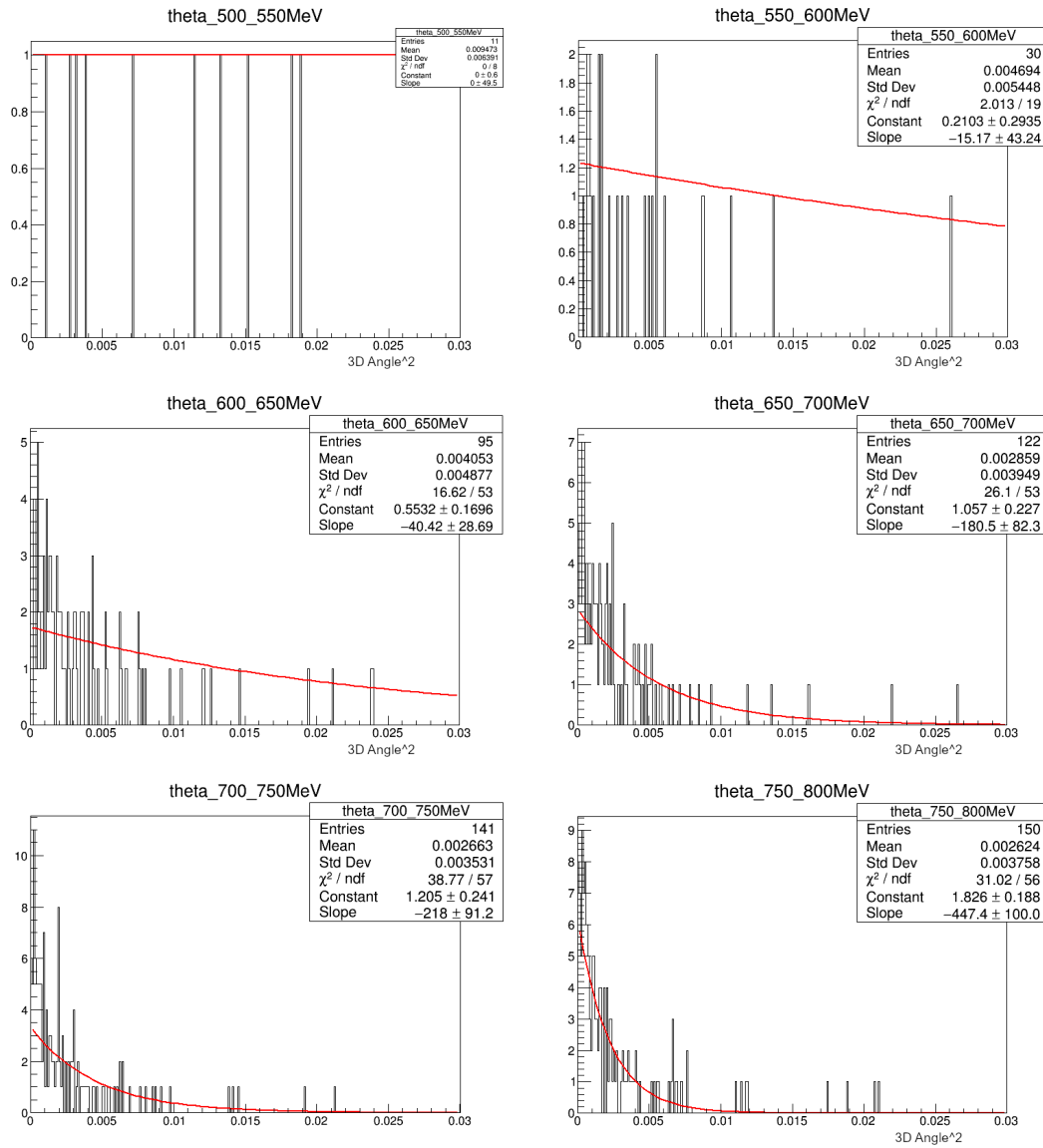
FIGURE 4.1: The distribution plot of the 3D Angle^2 for 500-800 *MeV/c* reconstructed data K$^+$ particles
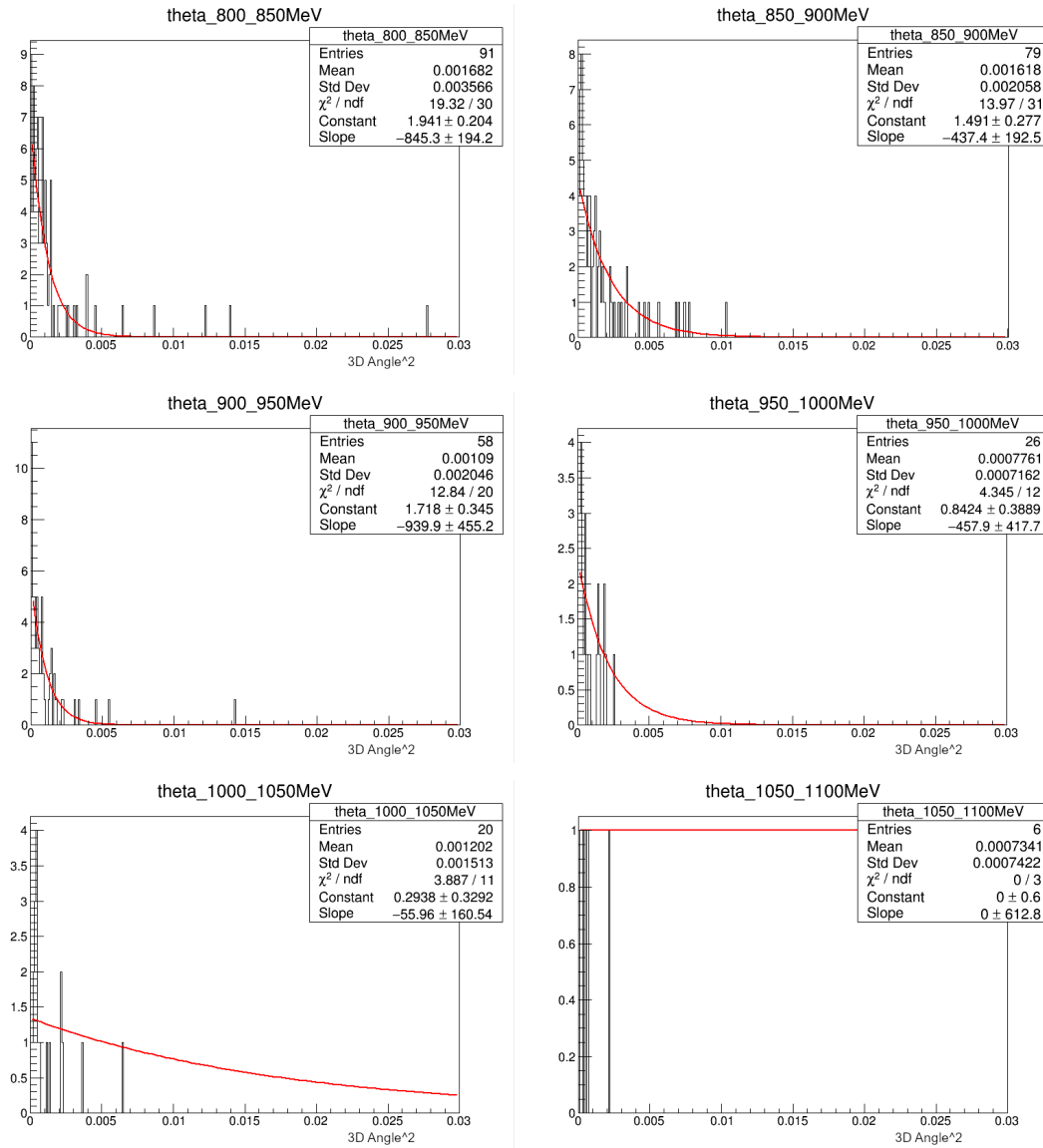
FIGURE 4.2: The distribution plot of the 3D Angle^2 for 800-1100 MeV/c reconstructed data K$^+$ particles
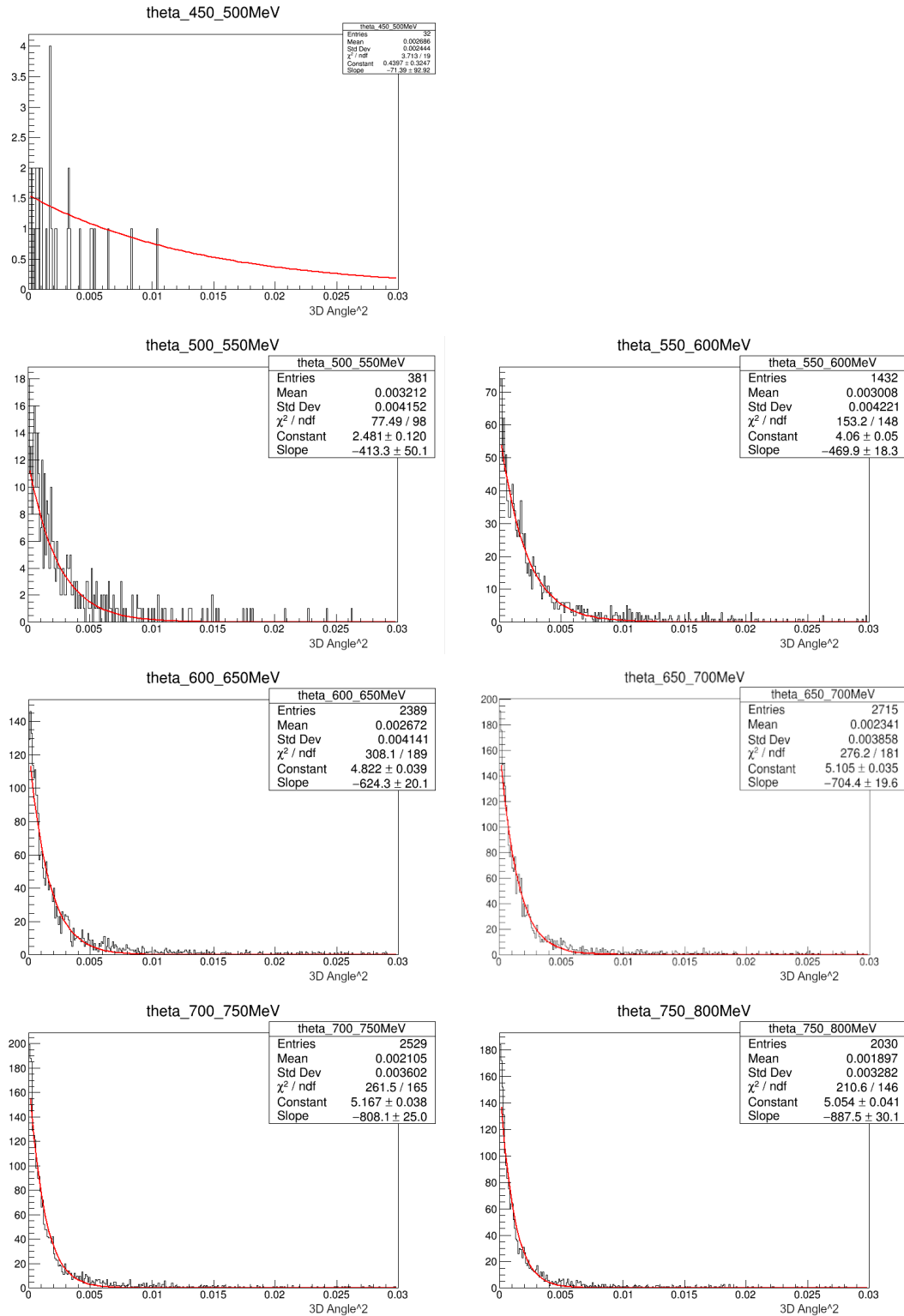
FIGURE 4.3: The distribution plot of the 3D Angle^2 for 450-800 *MeV/c* data particles consisting of about 18% μ^+ particles and about 82% π^+ particles
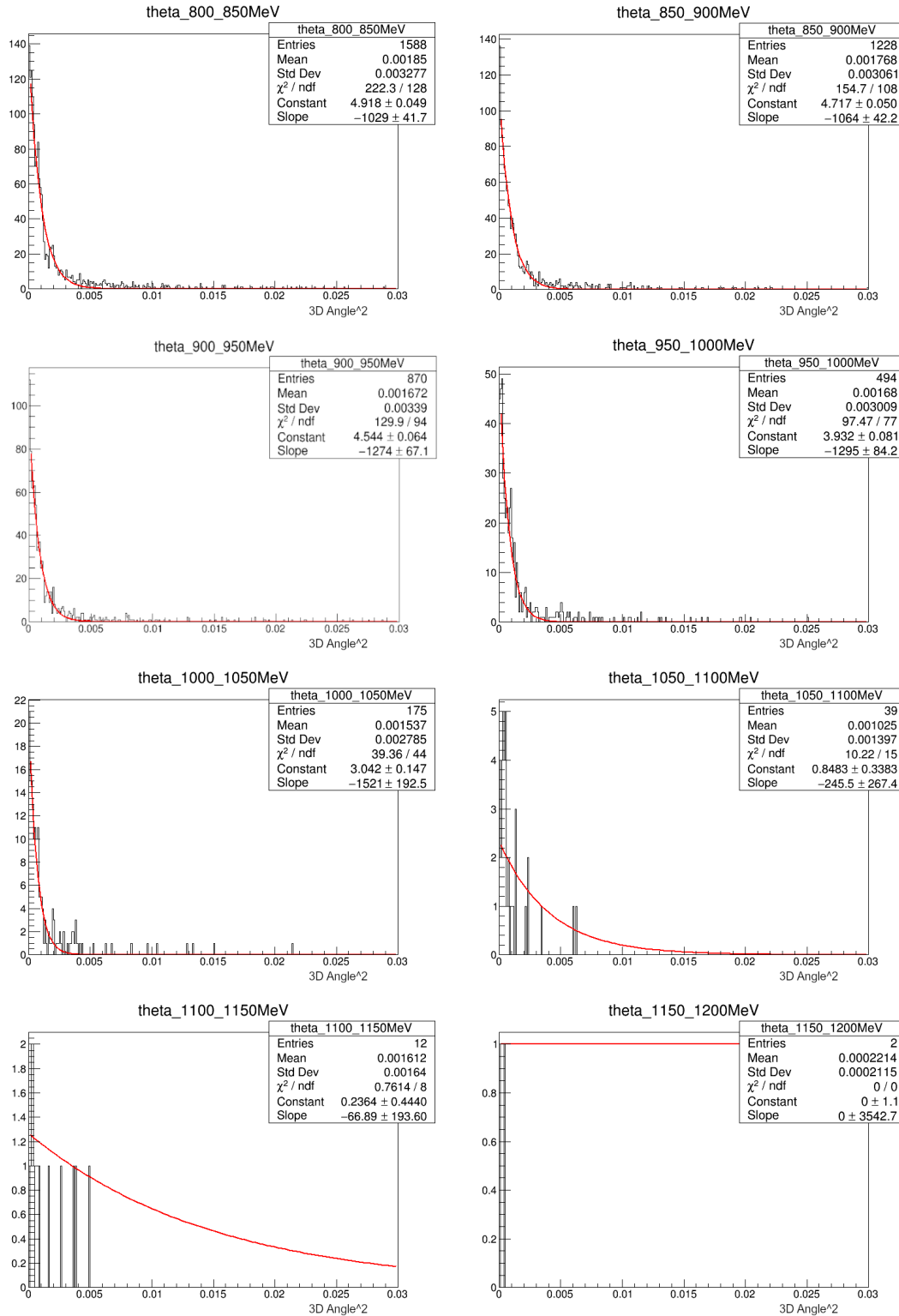
FIGURE 4.4: The distribution plot of the 3D Angle^2 for 800-1200 *MeV/c* data particles consisting of about 10% μ^+ particles and about 90% π^+ particles

FIGURE 4.5: The plot of standard deviation vs. particle track momentum per data particle with the nominal Highland formula and tuned Highland formula superimposed for comparison. The left figure is for data K^+ particles, and the right figure is for π^+/μ^+ particle data

4.5 Monte Carlo Results

In Figures 4.6-4.12, the distribution of the square of the 3D angle is plotted for each momentum range of each particle. The distribution is fit with an exponential function as outlined in Section 3.3 with fit parameters and errors listed in the table of each histogram. In Figure 4.14, the MCS standard deviations are plotted against each momentum bin for each particle. The x-coordinate of each point is taken to be the center of each momentum bin, with the bin width being the x error. The y error is calculated using Equation 3.14. The nominal Highland formula and tuned Highland formula curves are superimposed on each histogram for comparison to Monte Carlo. The tuned Highland formula for each particle uses the S_2^T constant collected from the fit of their respective data particle. The pion and kaon S_2^T values are 17.11 MeV and 17.38 MeV respectively. Monte Carlo particles that do not have a respective data fit, namely muons and protons, use $S_2^T = 17.245$ MeV, the average of the pion and kaon S_2^T values.
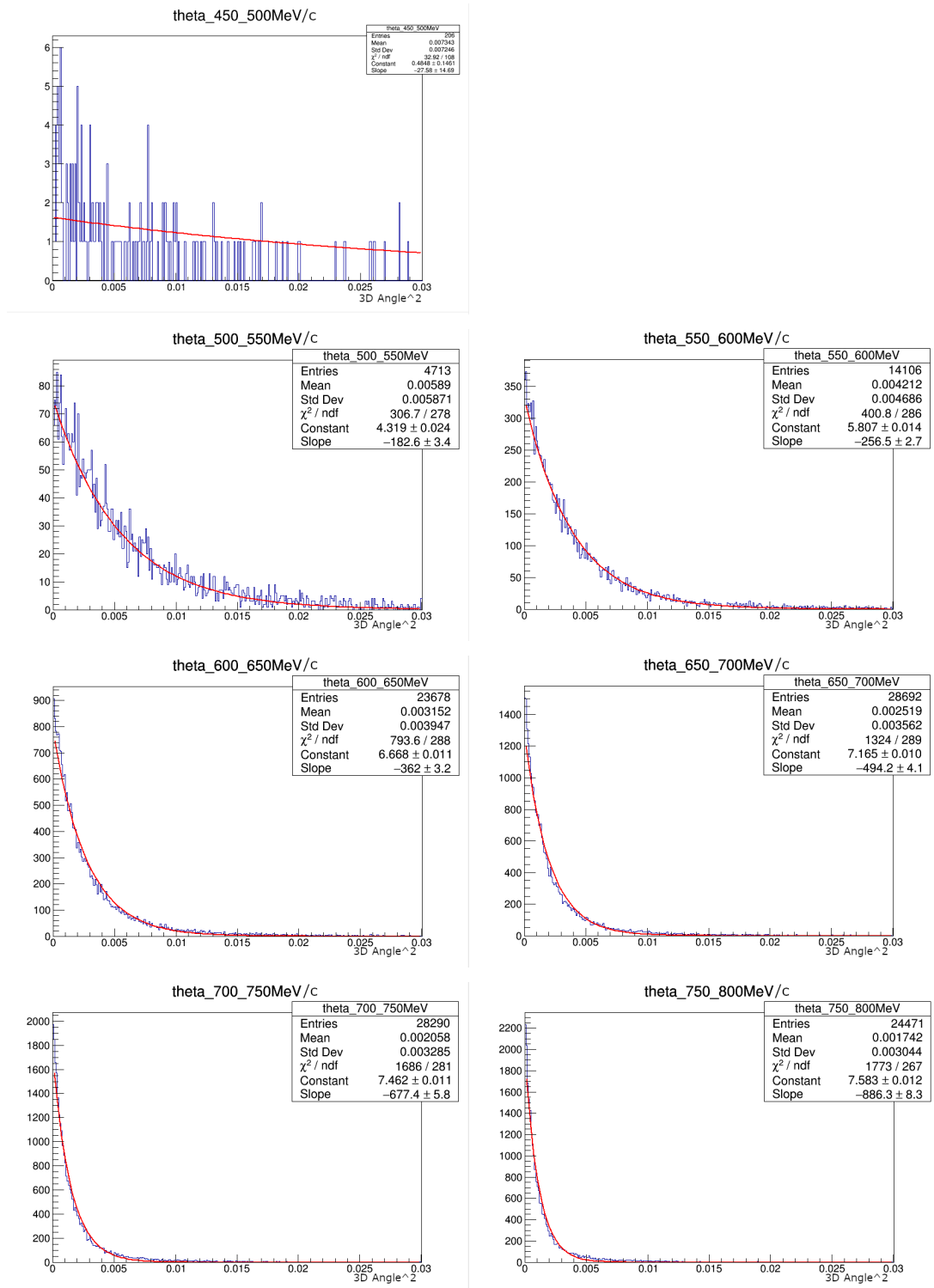
FIGURE 4.6: The distribution plot of the 3D Angle^2 for 450-800 *MeV/c* Monte Carlo simulated K$^+$ particles
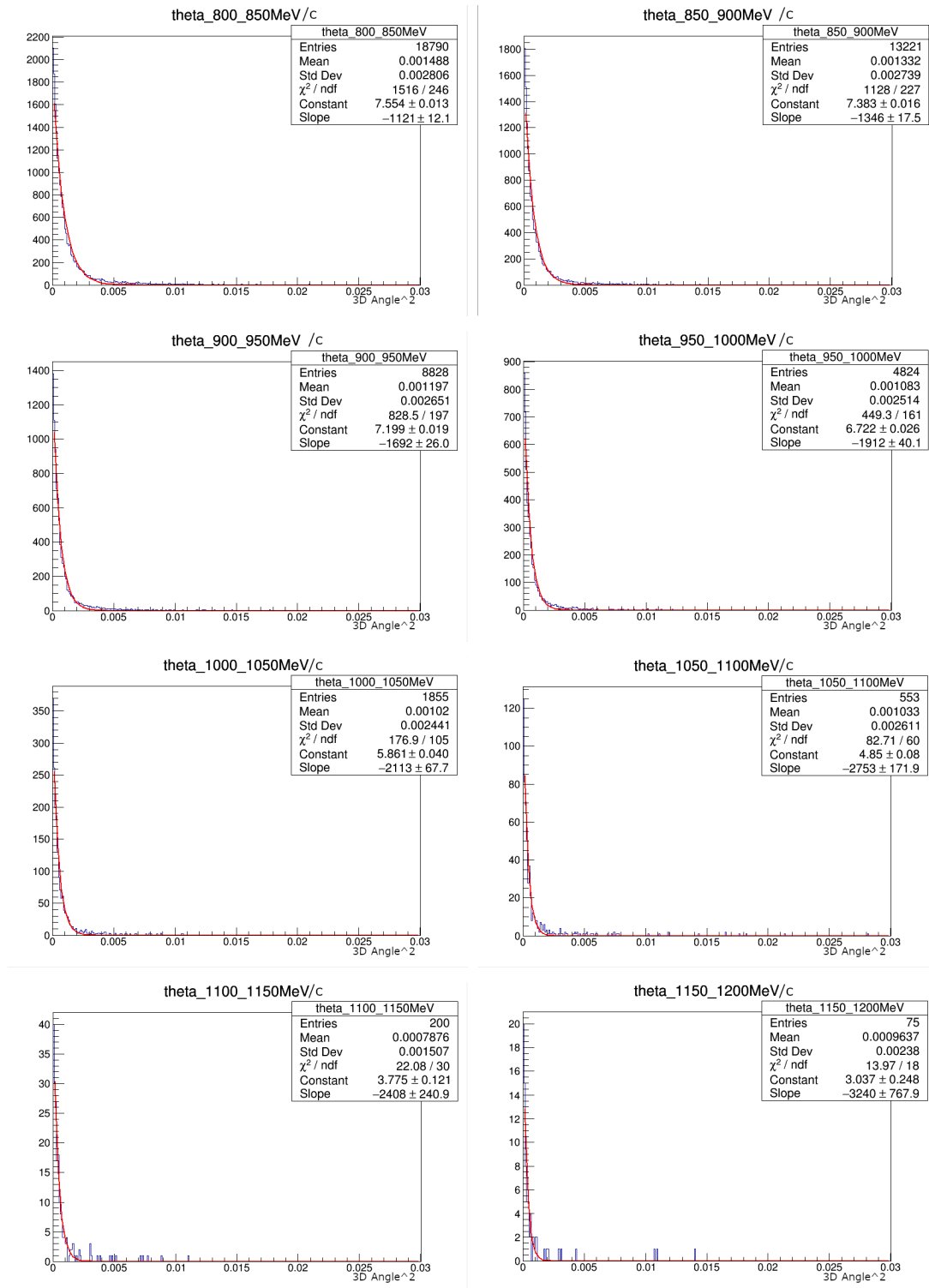
FIGURE 4.7: The distribution plot of the 3D Angle^2 for 800-1200 *MeV/c* Monte Carlo simulated K$^+$ particles
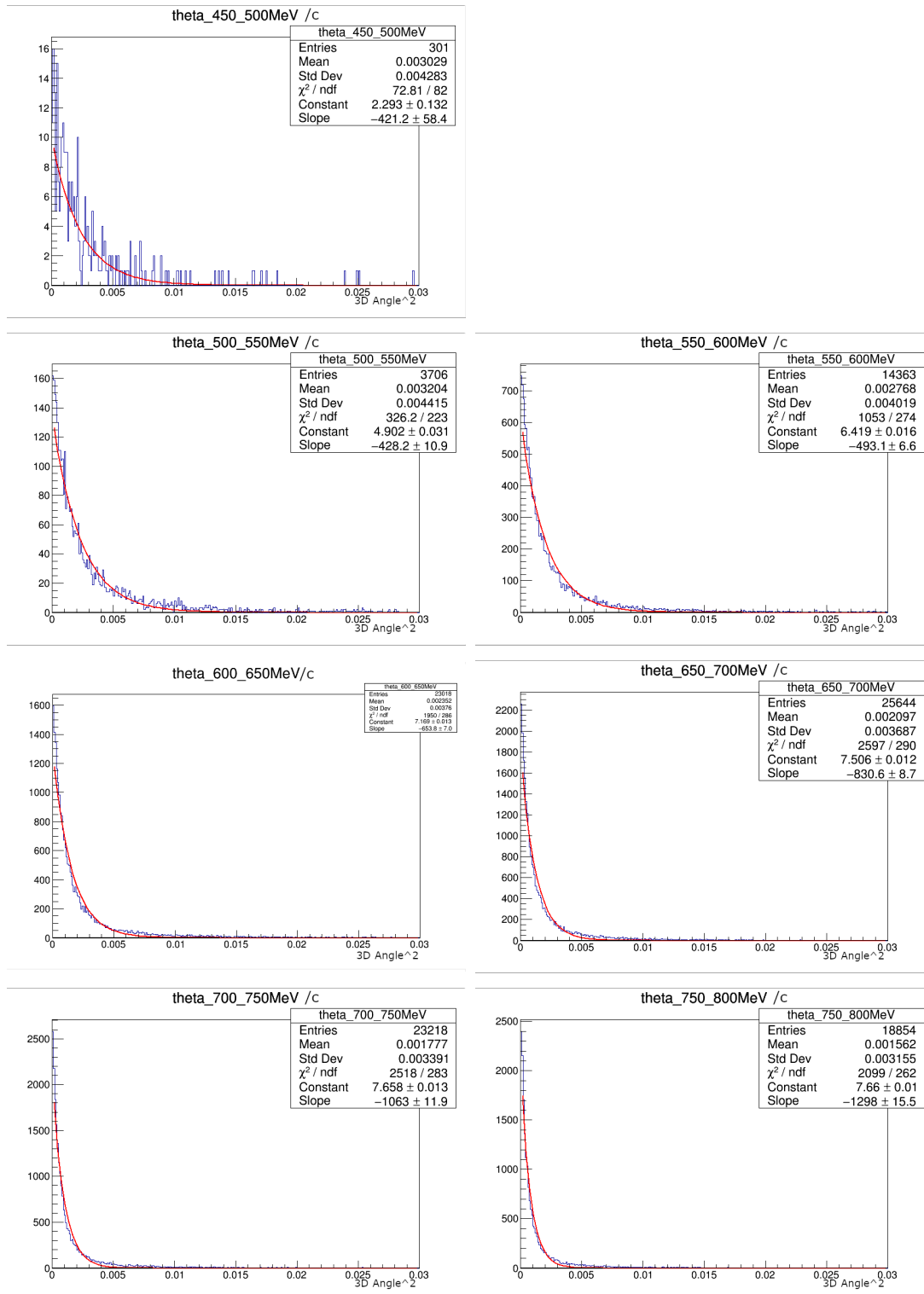
FIGURE 4.8: The distribution plot of the 3D Angle^2 for 450-800 MeV/c Monte Carlo simulated π^+ particles
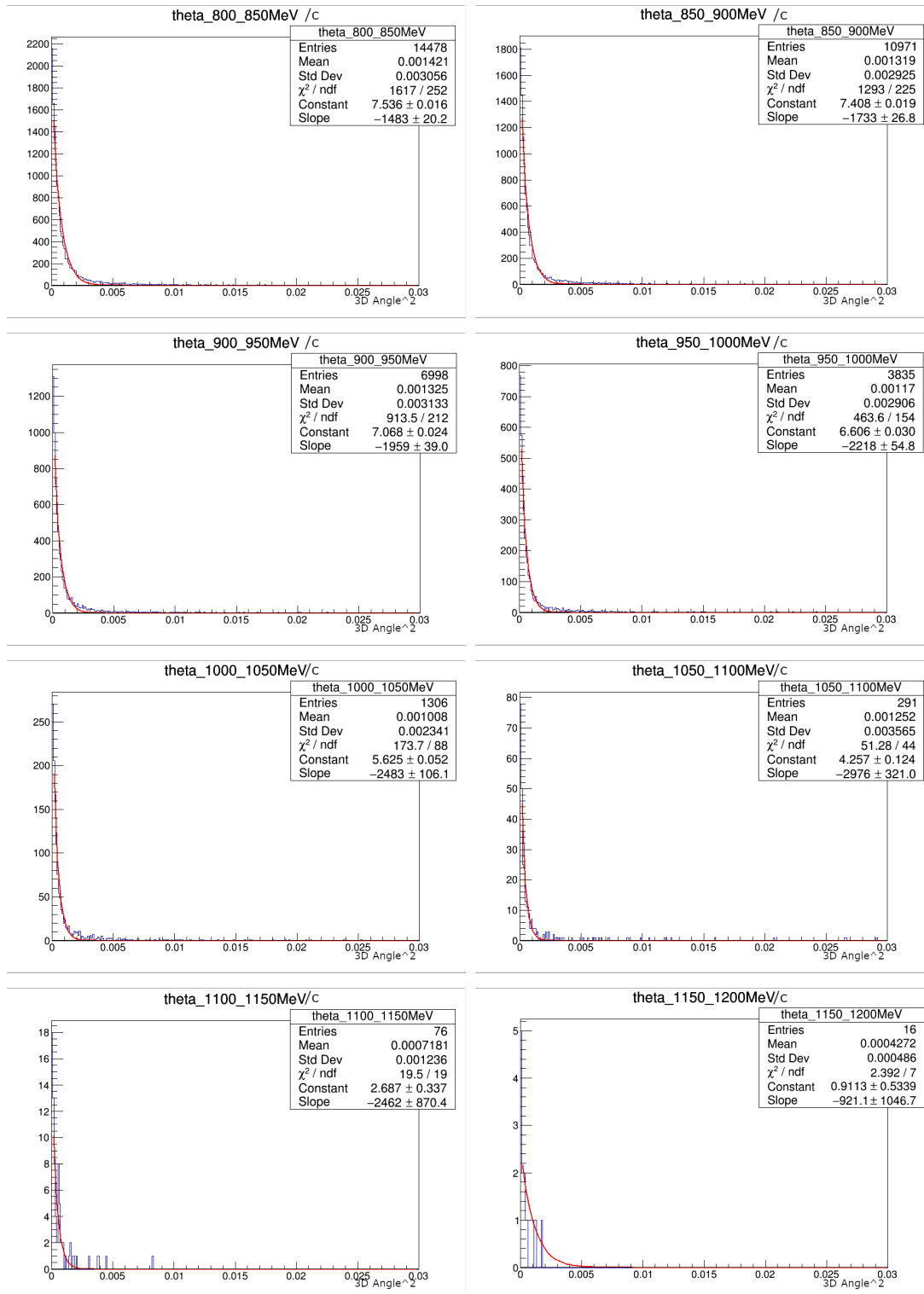
FIGURE 4.9: The distribution plot of the 3D Angle^2 for 800-1200 *MeV/c* Monte Carlo simulated π^+ particles
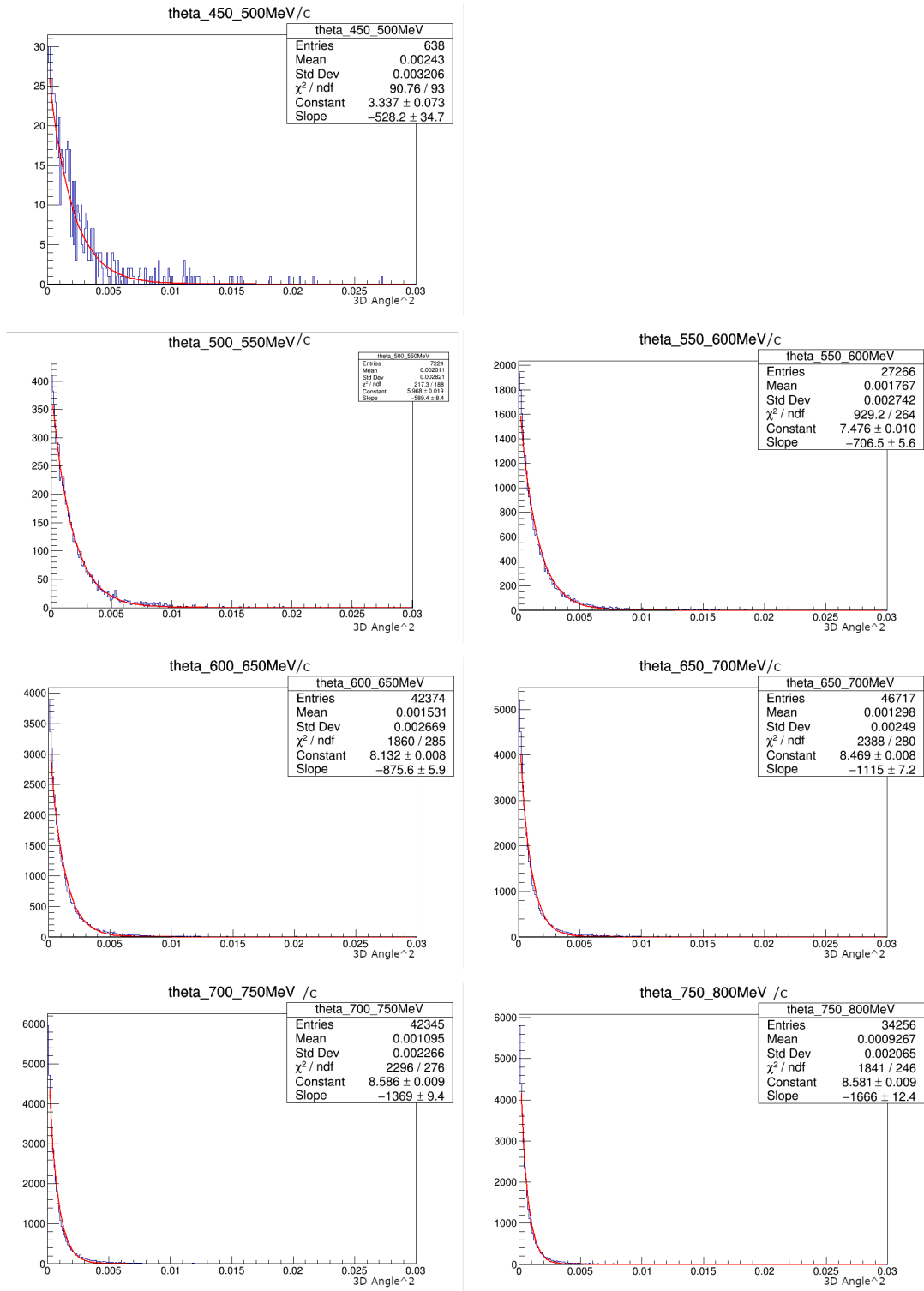
FIGURE 4.10: The distribution plot of the 3D Angle^2 for 450-800
MeV/c Monte Carlo simulated μ^+ particles
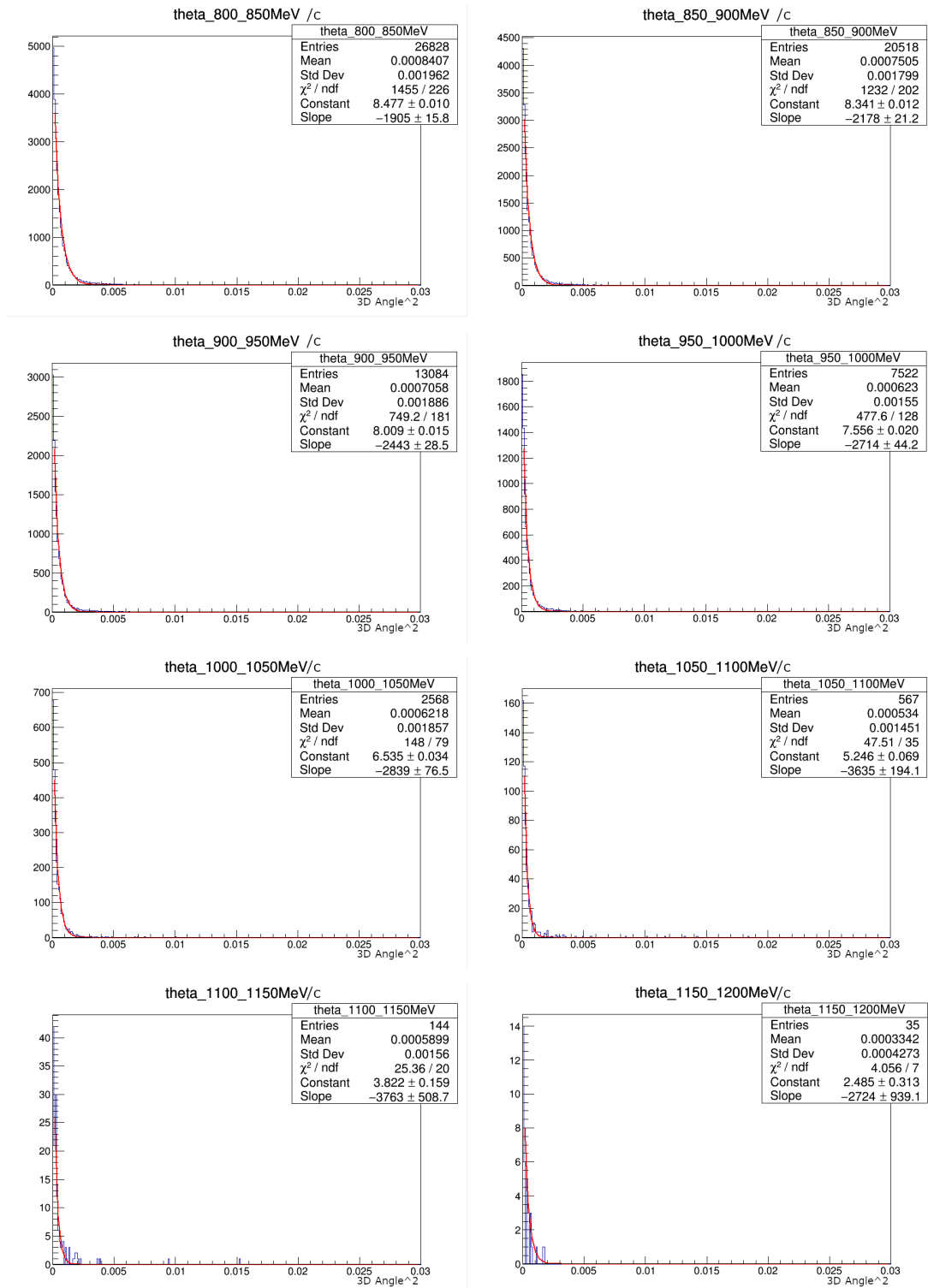
FIGURE 4.11: The distribution plot of the 3D Angle^2 for 800-1200 MeV/c Monte Carlo simulated μ^+ particles
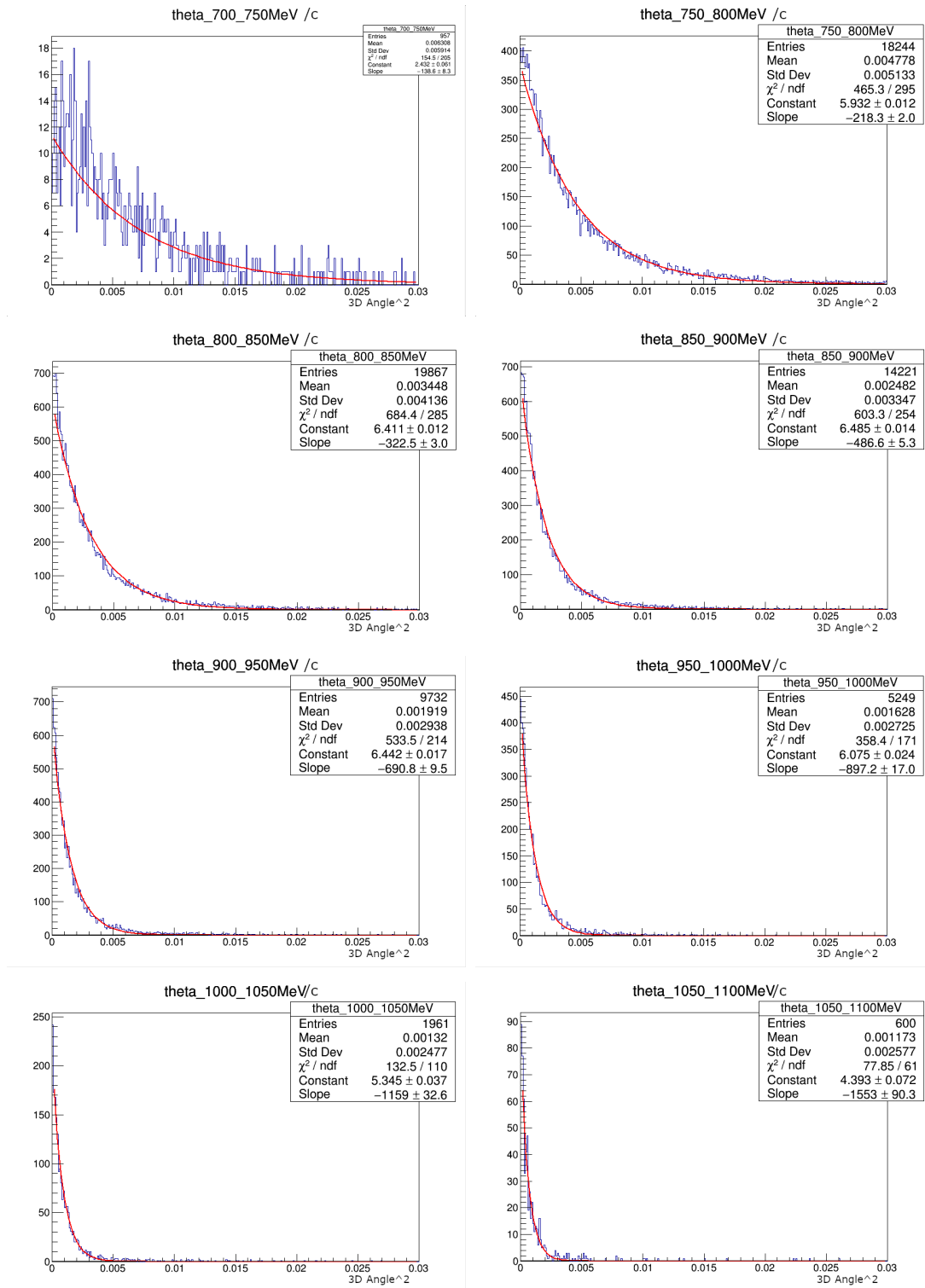
FIGURE 4.12: The distribution plot of the 3D Angle^2 for 700-1100 MeV/c Monte Carlo simulated protons
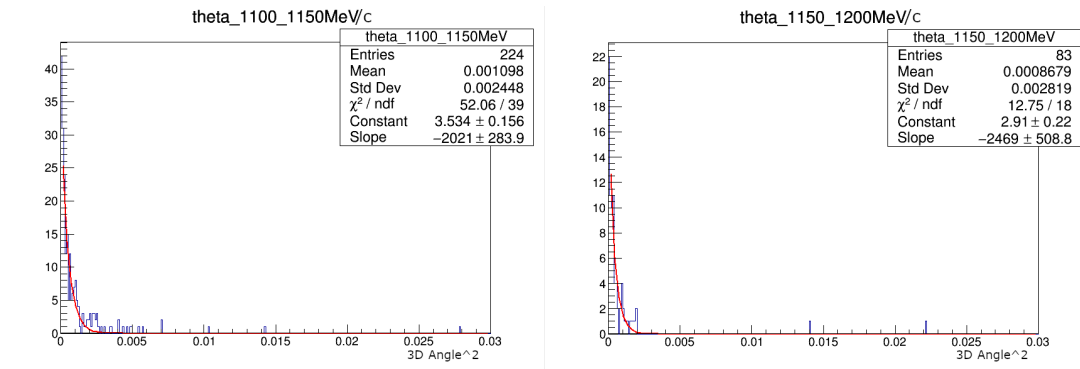
FIGURE 4.13: The distribution plot of the 3D Angle^2 for 1100-1200 MeV/c Monte Carlo simulated p particles
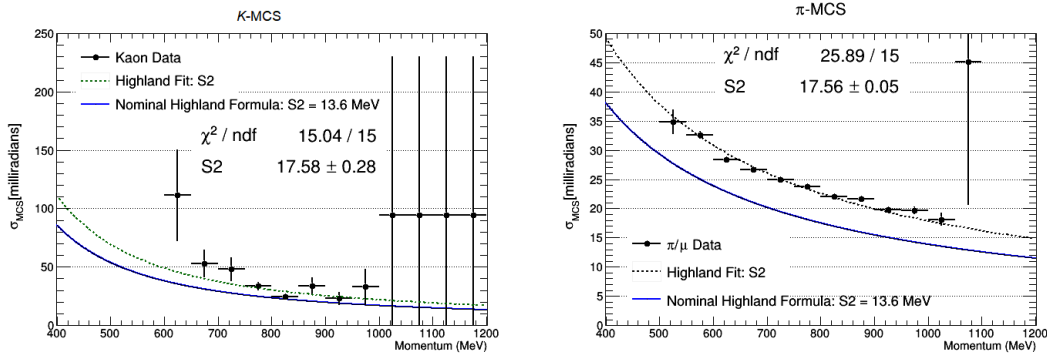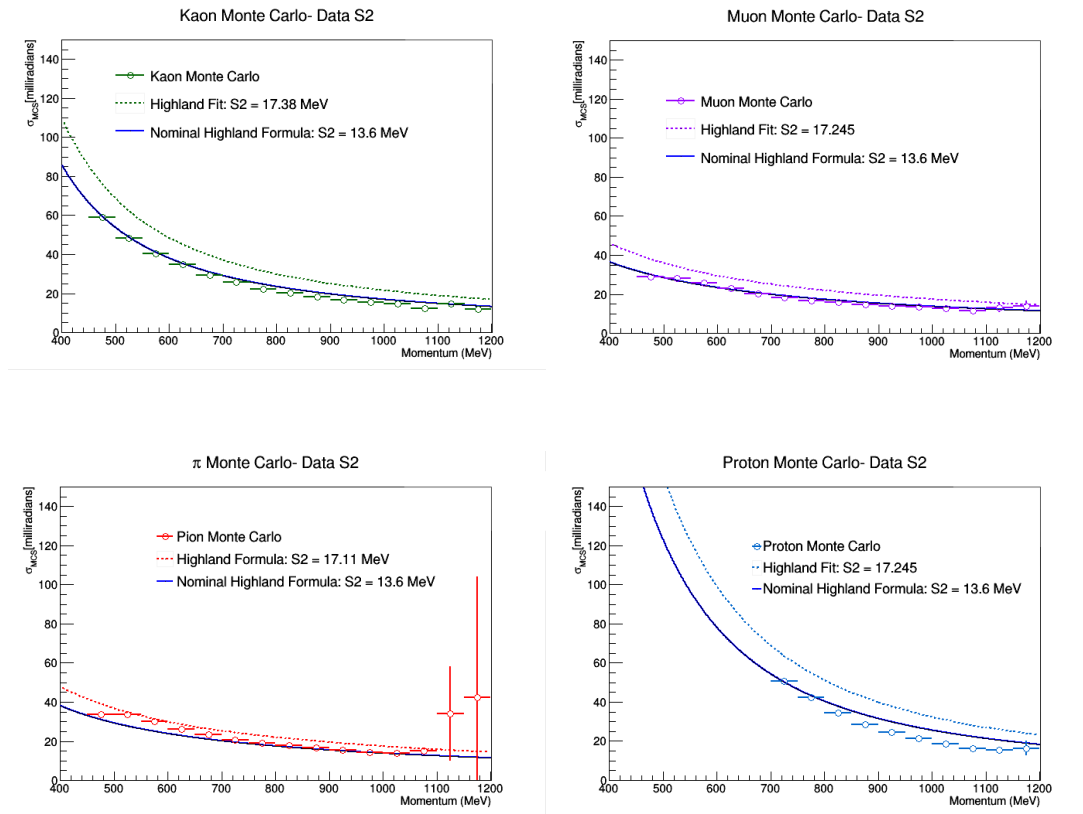
FIGURE 4.14: The plot of standard deviation vs. particle track momentum per Monte Carlo simulated particle with the nominal Highland formula and tuned Highland formula superimposed for comparison. The top-left figure is for Monte Carlo K^+ particles, top-right is for Monte Carlo μ^+ particles, bottom-left is for Monte Carlo π^+ particles, and bottom-right is for Monte Carlo p particles

Chapter 5

Discussion

In this chapter, the results of the error and χ^2/ndf accuracy analysis are presented, and we diagnose possible sources of error. We then discuss the fit of the tuned Highland formula as compared to the nominal Highland formula. Finally, we compare the results of the Monte Carlo exponential and Highland fits to those of the data. All errors are summarized in Table 5.1.

5.1   Error and Accuracy

Each exponential fit of a squared 3D angle distribution has an associated error, defined here as the tolerances of the constant and slope value, and an associated accuracy, defined here as the χ^2/ndf value.

Similarly, each tuned Highland fit σ_0 vs. momentum plot has an associated error, defined here as the tolerance of S_2, and an associated accuracy, defined here as the χ^2/ndf value. The x error bars on each point of the Highland comparison plots are given as the bin width. A 50 MeV span of momentum is the most precise the LArIAT detector hardware can measure at the time of this study. The y error bars on each point of the Highland comparison plots are calculated using Equation 3.14.

Some possible sources of error were poor statistics with small data samples especially for kaons, a slightly inaccurate estimated momentum value of each track, and an unadjusted exponential fit to the θ_{3D}^2 distribution. Each of

these are discussed more in detail in Chapter 6. There are also no statistics for proton data or muon data of acceptable purity, so the averaged S_2^T parameter used when calculating the tuned Highland formula with Monte Carlo simulation is slightly inaccurate. χ^2/ndf values for several θ_{3D}^2 plots were high, though we do not believe they had a significant effect on the final results.

5.2 Data vs. Monte Carlo Results
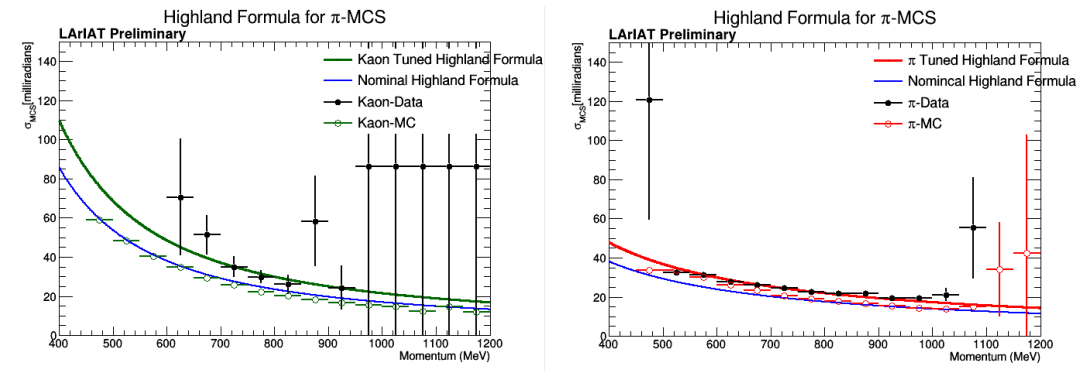
FIGURE 5.1: Plots of standard deviation vs. particle track momentum for both Monte Carlo and data particles with the nominal Highland formula and tuned Highland formula superimposed for comparison. The left figure is for K^+ particles, and the right figure is for π^+/μ^+ particles.

An interesting characteristic in the comparison between the data and Monte Carlo results is the significantly contrasting χ^2/ndf accuracy values for the fit of the tuned Highland formula. The χ^2/ndf values for data π^+/μ^+ and K^+ particles were 25.89/15 and 15.04/15 respectively. The S_2^T parameter in the tuned Highland formula was constructed with data, so the χ^2/ndf values for data show expected accuracy.
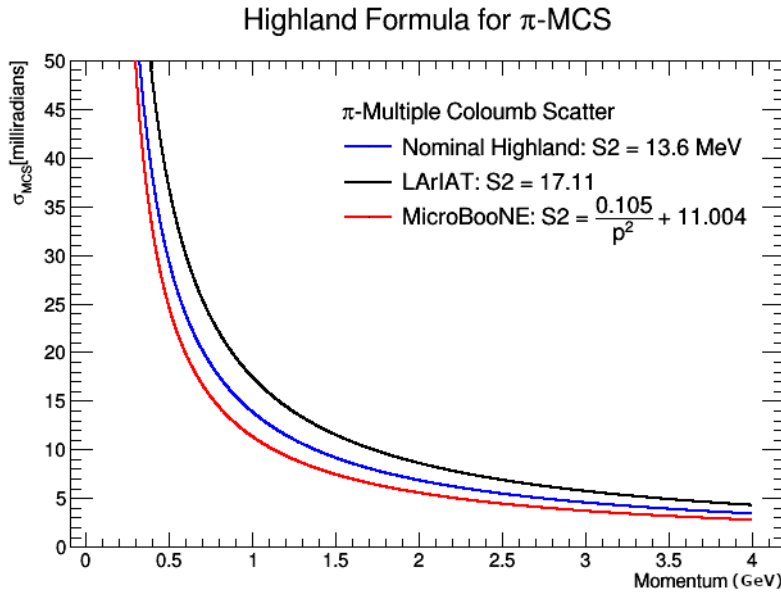
FIGURE 5.2: Comparison of the MicroBooNE tuned Highland formula using a paramaterized variation of S_2, the nominal Highland formula, and the LArIAT tuned Highland formula using the data-driven parameter S_2^T

5.3 Comparison to MicroBooNE Method

In an effort to validate our method, we both directly compared our results to the results of MicroBooNE's study[61] outlined in Section 3.2 and applied the MicroBooNE method to LArIAT data to measure accuracy.

Figure 5.2 shows the results of the direct comparison between the MicroBooNE curve generated by fitting their parameterized S_2 to Monte Carlo muon particles, the nominal Highland formula curve with S_2=13.6 MeV which has been used in the past for all particle types by default, and our tuned Highland curve using the data-driven muon S_2 value 17.11 MeV. The MicroBooNE curve underpredicts both our method and the nominal Highland formula.

Employing the MicroBooNE parameterization of the S_2 variable[61], we adjusted our tuned Highland curves for each particle type and plotted the π^+/μ^+ and K^+ data points on top. The results of this exercise can be seen in Figure 5.3. These results most notably align K^+ data with the predicted

Highland curve for protons and π^+/μ^+ with the predicted Highland curve for K^+. The LArIAT tuned Highland method used in our analysis is thus a more accurate characterization of particle data in LAr.
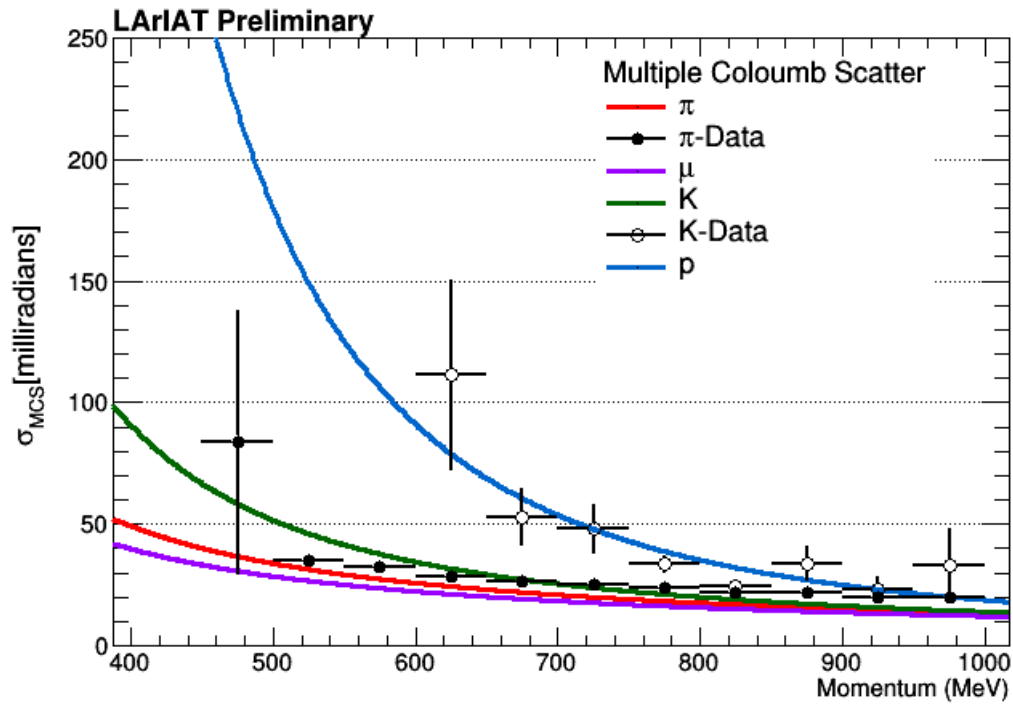
FIGURE 5.3: Comparison of π^+/μ^+ and K^+ data points with the tuned Highland curves for each particle type adjusted using the MicroBooNE S_2 parameterization

MC Pion	450-500 MeV/c	500-550 MeV/c	550-600 MeV/c	600-650 MeV/c	650-700 MeV/c	700-750 MeV/c	750-800 MeV/c	800-850 MeV/c	850-900 MeV/c	900-950 MeV/c	950-1000 MeV/c	1000-1050 MeV/c	1050-1100 MeV/c	1100-1150 MeV/c	1150-1200 MeV/c	Combined
S_2^T																17.11 ±0.02
Expo Constant	2.293 ±.132	4.902 ±.031	6.419 ±.016	7.169 ±.013	7.506 ±.012	7.658 ±.013	7.66 ±.01	7.536 ±.016	7.408 ±.019	7.068 ±.024	6.606 ±.030	5.625 ±.052	4.257 ±.124	2.687 ±.337	.9113 ±.5339	
Expo Slope	-421.2 ±58.4	-428.2 ±10.9	-493.1 ±6.6	-653.8 ±7.0	-830.6 ±8.7	-1063 ±11.9	-1298 ±15.5	-1483 ±20.2	-1733 ±26.8	-1959 ±39.0	-2218 ±54.8	-2483 ±106.1	-2976 ±321	-2462 ±870.4	-921.1 ±1046.7	
Expo χ^2/ndf	72.81/82	326.2/223	1053/274	1950/286	2597/290	2518/283	2099/262	1617/252	1293/225	913.5/212	463.6/154	173.7/88	51.28/44	19.5/19	2.392/7	
THL χ^2/ndf															2.177e+05/15	

| MC Kaon	450-500 MeV/c	500-550 MeV/c	550-600 MeV/c	600-650 MeV/c	650-700 MeV/c	700-750 MeV/c	750-800 MeV/c	800-850 MeV/c	850-900 MeV/c	900-950 MeV/c	950-1000 MeV/c	1000-1050 MeV/c	1050-1100 MeV/c	1100-1150 MeV/c	1150-1200 MeV/c	Combined
S_2^T																17.38 ± 1.14
Expo Constant	0.4848 ±.1461	4.319 ±.024	5.807 ±.014	6.668 ±.011	7.165 ±.01	7.462 ±.011	7.583 ±.012	7.554 ±.013	7.383 ±.016	7.199 ±.019	6.722 ±.026	5.861 ±.040	4.85 ±.08	3.775 ±.121	3.037 ±.248	
Expo Slope	-27.58 ±14.69	-182.6 ±3.4	-256.5 ±2.7	-362 ±3.2	-494.2 ±4.1	-677.4 ±5.8	-886.3 ±8.3	-1121 ±12.1	-1346 ±17.5	-1692 ±26.0	-1912 ±46.1	-2753 ±171.9	-3635 ±194.1	-2408 ±240.9	-3240 ±767.9	
Expo χ^2/ndf	32.92/108	306.7/278	400.8/286	793.6/288	1324/289	1686/281	1773/267	1516/246	1128/227	828.5/197	449.3/161	176.9/105	82.71/60	22.08/30	13.97/18	
THL χ^2/ndf															3.469e+05/15	

MC Muon	450-500 MeV/c	500-550 MeV/c	550-600 MeV/c	600-650 MeV/c	650-700 MeV/c	700-750 MeV/c	750-800 MeV/c	800-850 MeV/c	850-900 MeV/c	900-950 MeV/c	950-1000 MeV/c	1000-1050 MeV/c	1050-1100 MeV/c	1100-1150 MeV/c	1150-1200 MeV/c	Combined
S_2^T																17.245 ±0.142
Expo Constant	3.337 ±.073	5.968 ±.019	7.476 ±.010	8.132 ±.008	8.469 ±.008	8.586 ±.009	8.581 ±.009	8.477 ±.010	8.341 ±.012	8.009 ±.015	7.556 ±.020	6.535 ±.034	5.246 ±.069	3.822 ±.159	2.485 ±.313	
Expo Slope	-528.2 ±34.7	-589.4 ±8.4	-706.5 ±5.6	-875.6 ±5.9	-1115 ±7.2	-1369 ±9.4	-1666 ±12.4	-1905 ±15.8	-2178 ±21.2	-2443 ±28.5	-2714 ±44.2	-2839 ±76.5	-3635 ±194.1	-3763 ±508.7	-2724 ±939.1	
Expo χ^2/ndf	90.76/93	217.3/188	929.2/264	1860/285	2388/280	2296/276	1841/246	1455/226	1232/202	749.2/181	477.6/128	148/79	47.51/35	25.36/20	4.056/7	
THL χ^2/ndf															5.775e+05/15	

MC Proton	450-500 MeV/c	500-550 MeV/c	550-600 MeV/c	600-650 MeV/c	650-700 MeV/c	700-750 MeV/c	750-800 MeV/c	800-850 MeV/c	850-900 MeV/c	900-950 MeV/c	950-1000 MeV/c	1000-1050 MeV/c	1050-1100 MeV/c	1100-1150 MeV/c	1150-1200 MeV/c	Combined
S_2^T																17.245 ±0.142
Expo Constant						2.432 ±.061	5.932 ±.012	6.411 ±.012	6.485 ±.014	6.442 ±.017	6.075 ±.024	5.345 ±.037	4.393 ±.072	3.554 ±.156	2.91 ±.22	
Expo Slope						-138.6 ±8.3	-218.3 ±2.0	-322.5 ±3.0	-486.6 ±5.3	-690.8 ±9.5	-897.2 ±17.0	-1159 ±32.6	-1553 ±90.3	-2021 ±283.9	-2469 ±508.8	
Expo χ^2/ndf						154.5/205	465.3/295	684.4/285	603.3/254	533.5/214	358.4/171	132.5/110	77.85/61	52.06/39	12.75/18	
THL χ^2/ndf															1.675e+05/15	

Pi/Mu Data	450-500 MeV/c	500-550 MeV/c	550-600 MeV/c	600-650 MeV/c	650-700 MeV/c	700-750 MeV/c	750-800 MeV/c	800-850 MeV/c	850-900 MeV/c	900-950 MeV/c	950-1000 MeV/c	1000-1050 MeV/c	1050-1100 MeV/c	1100-1150 MeV/c	1150-1200 MeV/c	Combined
S_2^T																17.11 ±0.02
Expo Constant	.4397 ±.3247	2.481 ±.120	4.06 ±.05	4.822 ±.039	5.105 ±.035	5.167 ±.038	5.054 ±.041	4.918 ±.049	4.717 ±.050	4.544 ±.064	3.932 ±.081	3.042 ±.147	.8483 ±.3383	.2364 ±.4440	0 ±1.1	
Expo Slope	-71.39 ±92.92	-413.3 ±50.1	-469.9 ±18.3	-624.3 ±20.1	-704.4 ±19.6	-808.1 ±25.0	-887.5 ±30.1	-1029 ±41.7	-1064 ±42.2	-1274 ±67.1	-1295 ±84.2	-1521 ±192.5	-245.5 ±267.4	-66.89 ±193.60	0 ±3542.7	
Expo χ^2/ndf	3.713/19	77.49/98	153.2/148	308.1/189	276.2/181	261.5/165	210.6/146	222.3/128	154.7/108	129.9/94	97.47/77	39.36/44	10.22/15	.7614/8	0/0	
THL χ^2/ndf															40.07/15	

Kaon Data	450-500 MeV/c	500-550 MeV/c	550-600 MeV/c	600-650 MeV/c	650-700 MeV/c	700-750 MeV/c	750-800 MeV/c	800-850 MeV/c	850-900 MeV/c	900-950 MeV/c	950-1000 MeV/c	1000-1050 MeV/c	1050-1100 MeV/c	1100-1150 MeV/c	1150-1200 MeV/c	Combined
S_2^T																17.58 ±0.28
Expo Constant	0 ±.6	.2103 ±.2935	.5532 ±.1696	.5532 ±.1696	1.057 ±.227	1.205 ±.241	1.826 ±.188	1.941 ±.204	1.491 ±.277	1.718 ±.345	.8424 ±.3889	.2938 ±.3292	0 ±.6			
Expo Slope	0 ±49.5	-15.17 ±43.24	-40.42 ±28.69	-180.5 ±82.3	-218 ±91.2	-447.4 ±100.0	-845.3 ±194.2	-437.4 ±192.5	-939.9 ±455.2	-457.9 ±417.7	-55.96 ±160.54	0 ±612.8				
Expo χ^2/ndf	0/8	2.013/19	16.62/53	26.1/53	38.77/57	31.02/56	19.32/30	13.97/31	12.84/20	4.345/12	3.887/11	0/3				
THL χ^2/ndf															15.04/15	

TABLE 5.1: Error values for S_2^T, exponential fit constant, exponential fit slope, exponential fit χ^2/ndf, and tuned Highland χ^2/ndf for each particle type of both Monte Carlo and data

Chapter 6

Conclusion

This analysis has presented a characterization of κ^+, π^+, μ^+, and p multiple coulomb scattering as a function of incoming momentum and particle type. By fitting the squared 3D angle distribution with an exponential function, we were able to deduce the standard deviation σ^{HL}, which was then plotted against momentum. This curve was then compared to the nominal Highland function and fit with the tuned Highland function, where the S_2 parameter was uniquely defined as a function of particle type in LAr. Using this newly parameterized Highland equation that disagreed with the uniquely parameterized results found in a similar MicroBooNE study, we were able to attain a maximum χ^2/ndf inaccuracy to data of 25.89/15. This analysis presents an alternative technique for characterizing data in LArTPCs that more accurately predicts data particle behavior.

We made some necessary simplifications in this analysis that can be improved upon in future studies. The first of these simplifications was the momentum value, which was calculated from the value collected at wire chamber 4 and the estimated energy loss from the wire chamber to the point of intersection between the incoming and outgoing best fit lines. We believe the effect of this simplification is insignificant because it is small compared to the 50 MeV/c momentum bin size. A second simplification was the lack of refitting the exponential function to the squared 3D angle distribution. While this could be improved by adjusting fit limits and bin size in future studies,

our first fit was valid because the underlying distribution of the squared 3D angle is defined as exponential.

In the future, we plan to use this method in conjunction with proton data and larger data samples in general to further verify its accuracy. We hope that with more analyses, we may come closer to understanding the narrative behind the discrepancies in the Highland formulation between data and Monte Carlo particles.

Bibliography

[1] L.M. Brown. The idea of the neutrino. *Physics Today*, 31(9):23–28, 1978. URL https://physicstoday.scitation.org/doi/10.1063/1.2995181.

[2] David de Hilster. New radium e experiment. *Autodynamics*, 2013. URL http://www.autodynamics.org/new-radium-e-experiment/.

[3] S. M. Bilenky. Neutrino. History of a unique particle. *European Physical Journal H*, 38:345–404, May 2013. doi: 10.1140/epjh/e2012-20068-9.

[4] C. L. Cowan, F. Reines, F. B. Harrison, H. W. Kruse, and A. D. McGuire. Detection of the free neutrino: A Confirmation. *Science*, 124:103–104, 1956. doi: 10.1126/science.124.3212.103.

[5] F. Reines and C.L. Cowan. The neutrino. *Nature*, 178:446–449, 1956. URL https://www.nature.com/articles/178446a0.

[6] Bruce T. Cleveland, Timothy Daily, Jr. Raymond Davis, James R. Distel, Kenneth Lande, C. K. Lee, Paul S. Wildenhain, and Jack Ullman. Measurement of the solar electron neutrino flux with the homestake chlorine detector. *The Astrophysical Journal*, 496(1):505, 1998. URL http://stacks.iop.org/0004-637X/496/i=1/a=505.

[7] Raymond Davis. Solar neutrinos. ii. experimental. *Phys. Rev. Lett.*, 12: 303–305, Mar 1964. doi: 10.1103/PhysRevLett.12.303. URL https://link.aps.org/doi/10.1103/PhysRevLett.12.303.

[8] K. Lande, B. T. Cleveland, T. Daily, R. Davis, J. Distel, C. K. Lee, A. Weinberger, P. Wildenhain, and J. Ullman. Results from the Homestake solar neutrino observatory. *Conf. Proc.*, C900802:867–675, 1990. [Conf. Proc.C900802V1,C900802V1:667(1990)].

[9] J. N. Bahcall, M. H. Pinsonneault, and G. J. Wasserburg. Solar models with helium and heavy-element diffusion. *Reviews of Modern Physics*, 67: 781–808, October 1995. doi: 10.1103/RevModPhys.67.781.

[10] S. Turck-Chieze and I. Lopes. Toward a unified classical model of the sun - On the sensitivity of neutrinos and helioseismology to the microscopic physics. *apj*, 408:347–367, May 1993. doi: 10.1086/172592.

[11] I.-J. Sackmann, A. I. Boothroyd, and W. A. Fowler. Our sun. I - The standard model: Successes and failures. *apj*, 360:727–736, sep 1990. doi: 10.1086/169158.

[12] R. Jeffrey Wilkes. Evidence for neutrino oscillation from Super-Kamiokande. In *Results and perspectives in particle physics. Proceedings, Les Rencontres de Physique de la Vallee d'Aoste, La Thuile, Italy, March 1 - 7, 1998*, pages pp.73–91, 1994.

[13] Alan Chodos. New SNO Data Resolves Solar Neutrino Problem. *American Physical Society*, 11(6), 2002. URL https://www.aps.org/publications/apsnews/200206/sno.cfm.

[14] Y. Grossman and H. J. Lipkin. Flavor oscillations from a spatially localized source: A simple general treatment. *Phys. Rev. D*, 55:2760–2767, March 1997. doi: 10.1103/PhysRevD.55.2760.

[15] S. Bilenky. Neutrino oscillations: From a historical perspective to the present status. *Nuclear Physics B*, 908:2–13, July 2016. doi: 10.1016/j.nuclphysb.2016.01.025.

[16] T. Kajita. Atmospheric neutrinos. *New Journal of Physics*, 6:194, December 2004. doi: 10.1088/1367-2630/6/1/194.

[17] K. Abe, N. Abgrall, H. Aihara, Y. Ajima, J. B. Albert, D. Allan, P.-A. Amaudruz, C. Andreopoulos, B. Andrieu, M. D. Anerella, and et al. The T2K experiment. *Nuclear Instruments and Methods in Physics Research A*, 659:106–135, December 2011. doi: 10.1016/j.nima.2011.06.067.

[18] Y. Itow, T. Kajita, K. Kaneyuki, M. Shiozawa, Y. Totsuka, Y. Hayato, T. Ishida, T. Ishii, T. Kobayashi, T. Maruyama, K. Nakamura, Y. Obayashi, Y. Oyama, M. Sakuda, M. Yoshida, S. Aoki, T. Hara, A. Suzuki, A. Ichikawa, T. Nakaya, K. Nishikawa, T. Hasegawa, K. Ishihara, A. Suzuki, and A. Konaka. The JHF-Kamioka neutrino project. *ArXiv High Energy Physics - Experiment e-prints*, June 2001.

[19] Takaaki Kajita. Atmospheric neutrinos. *New Journal of Physics*, 6(1):194, 2004. URL http://stacks.iop.org/1367-2630/6/i=1/a=194.

[20] Y. Fukuda et al. The Super-Kamiokande detector. *Nucl. Instrum. Meth.*, A501:418–462, 2003. doi: 10.1016/S0168-9002(03)00425-X.

[21] Y. Fukuda and et al. Evidence for oscillation of atmospheric neutrinos. *Phys. Rev. Lett.*, 81:1562–1567, Aug 1998. doi: 10.1103/PhysRevLett.81.1562. URL https://link.aps.org/doi/10.1103/PhysRevLett.81.1562.

[22] Y. Fukuda and et al. Measurements of the solar neutrino flux from super-kamiokande's first 300 days. *Phys. Rev. Lett.*, 81:1158–1162, Aug 1998. doi: 10.1103/PhysRevLett.81.1158. URL https://link.aps.org/doi/10.1103/PhysRevLett.81.1158.

[23] Y. Fukuda and et al. Measurement of the solar neutrino energy spectrum using neutrino-electron scattering. *Phys. Rev. Lett.*, 82:2430–2434, Mar 1999. doi: 10.1103/PhysRevLett.82.2430. URL https://link.aps.org/doi/10.1103/PhysRevLett.82.2430.

[24] M. Shiozawa and et al. Search for proton decay via $p \rightarrow e^+ \beta^0$ in a large water cherenkov detector. *Phys. Rev. Lett.*, 81:3319–3323, Oct 1998. doi: 10.1103/PhysRevLett.81.3319. URL https://link.aps.org/doi/10.1103/PhysRevLett.81.3319.

[25] Y. Hayato and et al. Search for proton decay through $p \rightarrow \bar{\circ}k^+$ in a large water cherenkov detector. *Phys. Rev. Lett.*, 83:1529–1533, Aug 1999. doi: 10.1103/PhysRevLett.83.1529. URL https://link.aps.org/doi/10.1103/PhysRevLett.83.1529.

[26] D. Kalra. Current Status for the Inclusive Neutral Current π^0 production Cross Section Measurement with the NOvA Near Detector. *ArXiv e-prints*, October 2017.

[27] B. Gabioud and et al. Measurement of ionization loss in the relativistic rise region with the time projection chamber. *IEEE Transactions on Nuclear Science*, 30(1):63–66, Feb 1983. ISSN 0018-9499. doi: 10.1109/TNS.1983.4332220.

[28] J. Asaadi M. Backfish W. Badgett B. Baller F. d. M. Blaszczyk R. Bouabid Bromberg R. Carey F. Cavanna A. Chatterjee M. V. dos Santos D. Edmunds. M. Elkins J. Esquivel J. Evans A. Falcone A. Farbin R. C. Fernandez W. Flanagan B. Fleming W. Foreman D. Garcia-Gamez D. Gastler B. Gelli T. Ghosh R. A. Gomes E. Gramellini R. Gran D. R. Gratieri P. Guzowski A. Habig A. Hahn P. Hamilton C. Hill J. Ho A. Holin J. Hugon E. Iwai D. Jensen R. Johnson H. Jostlein E. Kearns E. Kemp M. Kirby T. Kobilarcik M. Kordosky P. Kryczyński K. Lang R. Linehan S. Lockwitz X. Luo A. Marchionni T. Maruyama L. M. Santos W. Metcalf C. A. Moura R. Nichol M. S. Nunes I. Nutini A. Olivier O. Palamara J. Paley I. Parmaksiz L. Paulucci D. Phan G. Pulliam J. L. Raaf B. Rebel M. Reggiani-Guzzo O. Rodrigues M. Ross-Lonergan D. Schmitz E. Segreto D. Sessumes S. Shahsavarani D. Shooltz D. Smith M. Soderberg B. Soubasis J. St. John M. Stancari D. Stefan M. Stephens R. Sulej A. Szelc M. Tzanov G. A. Valdiviesso Z. Williams T. Yang J. Yu G. P. Zeller S. Zhang J. Zhu R. Acciarri, C. Adams. The Liquid Argon In A Testbeam (LArIAT) Experiment. Technical report, Fermi National Accelerator Laboratory, 11 2018.

[29] S. Amerio et al. Design, construction and tests of the ICARUS T600 detector. *Nucl. Instrum. Meth.*, A527:329–410, 2004. doi: 10.1016/j.nima.2004.02.044.

[30] C. Rubbia et al. Underground operation of the ICARUS T600 LArTPC: first results. *JINST*, 6:P07011, 2011. doi: 10.1088/1748-0221/6/07/P07011.

[31] C. Anderson et al. The ArgoNeuT Detector in the NuMI Low-Energy beam line at Fermilab. *JINST*, 7:P10019, 2012. doi: 10.1088/1748-0221/7/10/P10019.

[32] K. Anderson et al. The NuMI Facility Technical Design Report. 1998.

[33] C. Anderson et al. First Measurements of Inclusive Muon Neutrino Charged Current Differential Cross Sections on Argon. *Phys. Rev. Lett.*, 108:161802, 2012. doi: 10.1103/PhysRevLett.108.161802.

[34] R. Acciarri et al. First Observation of Low Energy Electron Neutrinos in a Liquid Argon Time Projection Chamber. *Phys. Rev.*, D95(7):072005, 2017. doi: 10.1103/PhysRevD.95.072005. [Phys. Rev.D95,072005(2017)].

[35] R. Acciarri et al. Measurement of ν_μ and $\bar{\nu}_\mu$ neutral current $\pi^0 \to \gamma\gamma$ production in the ArgoNeuT detector. *Phys. Rev.*, D96(1):012006, 2017. doi: 10.1103/PhysRevD.96.012006.

[36] R. Acciarri et al. First Measurement of Neutrino and Antineutrino Coherent Charged Pion Production on Argon. *Phys. Rev. Lett.*, 113(26):261801, 2014. doi: 10.1103/PhysRevLett.113. 261801,10.1103/PhysRevLett.114.039901. [erratum: Phys. Rev. Lett.114,no.3,039901(2015)].

[37] R. Acciarri et al. Detection of Back-to-Back Proton Pairs in Charged-Current Neutrino Interactions with the ArgoNeuT Detector in the NuMI Low Energy Beam Line. *Phys. Rev.*, D90(1):012008, 2014. doi: 10.1103/ PhysRevD.90.012008.

[38] R. Acciarri et al. Measurements of Inclusive Muon Neutrino and Antineutrino Charged Current Differential Cross Sections on Argon in the NuMI Antineutrino Beam. *Phys. Rev.*, D89(11):112003, 2014. doi: 10.1103/PhysRevD.89.112003.

[39] C. Anderson et al. Analysis of a Large Sample of Neutrino-Induced Muons with the ArgoNeuT Detector. *JINST*, 7:P10020, 2012. doi: 10. 1088/1748-0221/7/10/P10020.

[40] R. Acciarri et al. A study of electron recombination using highly ionizing particles in the ArgoNeuT Liquid Argon TPC. *JINST*, 8:P08005, 2013. doi: 10.1088/1748-0221/8/08/P08005.

[41] A. Aguilar-Arevalo et al. Evidence for neutrino oscillations from the observation of anti-neutrino(electron) appearance in a anti-neutrino(muon) beam. *Phys. Rev.*, D64:112007, 2001. doi: 10.1103/ PhysRevD.64.112007.

[42] A. A. Aguilar-Arevalo et al. A Search for Electron Antineutrino Appearance at the $\Delta m^2 \sim 1$ eV^2 Scale. *Phys. Rev. Lett.*, 103:111801, 2009. doi: 10.1103/PhysRevLett.103.111801.

[43] R. Acciarri et al. Design and Construction of the MicroBooNE Detector. *JINST*, 12(02):P02017, 2017. doi: 10.1088/1748-0221/12/02/P02017.

[44] R. Acciarri et al. Long-Baseline Neutrino Facility (LBNF) and Deep Underground Neutrino Experiment (DUNE). 2016.

[45] R. Acciarri et al. Long-Baseline Neutrino Facility (LBNF) and Deep Underground Neutrino Experiment (DUNE). 2015.

[46] James Strait et al. Long-Baseline Neutrino Facility (LBNF) and Deep Underground Neutrino Experiment (DUNE). 2016.

[47] R. Acciarri et al. Long-Baseline Neutrino Facility (LBNF) and Deep Underground Neutrino Experiment (DUNE). 2016.

[48] L. Alvarez-Ruso et al. NuSTEC White Paper: Status and Challenges of Neutrino-Nucleus Scattering. 2017.

[49] G. W. Bennett et al. Final Report of the Muon E821 Anomalous Magnetic Moment Measurement at BNL. *Phys. Rev.*, D73:072003, 2006. doi: 10.1103/PhysRevD.73.072003.

[50] H Fenker. Standard beam pwc for fermilab. Technical report, Fermi National Accelerator Lab., Batavia, IL (USA), 1983.

[51] David A. Sanders. MICE Particle Identification Systems. page TU6RFP065, 2010. [Conf. Proc.C090504,1696(2009)].

[52] S. Nishida, I. Adachi, N. Hamada, K. Hara, T. Iijima, S. Iwata, H. Kakuno, H. Kawai, S. Korpar, P. Krizan, S. Ogawa, R. Pestotnik, L. Santelj, A. Seljak, T. Sumiyoshi, M. Tabata, E. Tahirovic, K. Yoshida, and Y. Yusa. Aerogel rich for the belle ii forward pid. *Nuclear Instruments and Methods in Physics Research Section A: Accelerators, Spectrometers, Detectors and Associated Equipment*, 766:28 − 31, 2014. ISSN 0168-9002. doi: https://doi.org/10.1016/j.nima.2014.06.061. URL http://www.sciencedirect.com/science/article/pii/S0168900214008080. RICH2013 Proceedings of the Eighth International Workshop on Ring Imaging Cherenkov Detectors Shonan, Kanagawa, Japan, December 2-6, 2013.

[53] J. Asaadi, J. M. Conrad, S. Gollapinni, B. J. P. Jones, H. Jostlein, J. M. St. John, T. Strauss, S. Wolbers, and J. Zennamo. Testing of High Voltage Surge Protection Devices for Use in Liquid Argon TPC Detectors. *JINST*, 9:P09002, 2014. doi: 10.1088/1748-0221/9/09/P09002.

[54] E. Snider. Introduction to LArSoft. Technical report, Fermi National Accelerator Laboratory, 8 2015.

[55] E. Rutherford. The Scattering of alpha and beta Particles by Matter and the Structure of the Atom. *Philosophical Magazine*, 21(6):669–688, 1911.

[56] G. Molière. Theorie der Streuung schneller geladener Teilchen II. Mehrfach- und Vielfachstreuung. *Zeitschrift Naturforschung Teil A*, 3:78–97, February 1948. doi: 10.1515/zna-1948-0203.

[57] G.R. Lynch and O.I. Dahl. Beam Interactions with Materials and Atoms. *Nucl. Instrum. Methods*, 1991.

[58] P. Abratenko, R. Acciarri, C. Adams, R. An, J. Anthony, J. Asaadi, M. Auger, L. Bagby, S. Balasubramanian, B. Baller, C. Barnes, G. Barr, M. Bass, F. Bay, M. Bishai, A. Blake, T. Bolton, L. Bugel, L. Camilleri, D. Caratelli, B. Carls, R. Castillo Fernandez, F. Cavanna, H. Chen, E. Church, D. Cianci, E. Cohen, G. H. Collin, J. M. Conrad, M. Convery, J. I. Crespo-Anadón, M. Del Tutto, D. Devitt, S. Dytman, B. Eberly, A. Ereditato, L. Escudero Sanchez, J. Esquivel, B. T. Fleming, W. Foreman, A. P. Furmanski, D. Garcia-Gamez, G. T. Garvey, V. Genty, D. Goeldi, S. Gollapinni, N. Graf, E. Gramellini, H. Greenlee, R. Grosso, R. Guenette, A. Hackenburg, P. Hamilton, O. Hen, J. Hewes, C. Hill, J. Ho, G. Horton-Smith, E.-C. Huang, C. James, J. J. de Vries, C.-M. Jen, L. Jiang, R. A. Johnson, J. Joshi, H. Jostlein, D. Kaleko, L. N. Kalousis, G. Karagiorgi, W. Ketchum, B. Kirby, M. Kirby, T. Kobilarcik, I. Kreslo, A. Laube, Y. Li, A. Lister, B. R. Littlejohn, S. Lockwitz, D. Lorca, W. C. Louis, M. Luethi, B. Lundberg, X. Luo, A. Marchionni, C. Mariani, J. Marshall, D. A. Martinez Caicedo, V. Meddage, T. Miceli, G. B. Mills, J. Moon, M. Mooney, C. D. Moore, J. Mousseau, R. Murrells, D. Naples, P. Nienaber, J. Nowak, O. Palamara, V. Paolone, V. Papavassiliou, S. F. Pate, Z. Pavlovic, E. Piasetzky, D. Porzio, G. Pulliam, X. Qian, J. L. Raaf, A. Rafique, L. Rochester, C. R. von Rohr, B. Russell, D. W. Schmitz, A. Schukraft, W. Seligman, M. H. Shaevitz, J. Sinclair, E. L. Snider, M. Soderberg, S. Söldner-Rembold, S. R. Soleti, P. Spentzouris, J. Spitz, J. St. John, T. Strauss, A. M. Szelc, N. Tagg, K. Terao, M. Thomson, M. Toups, Y.-T. Tsai, S. Tufanli, T. Usher, R. G. Van de Water, B. Viren, M. Weber, D. A. Wickremasinghe, S. Wolbers, T. Wongjirad, K. Woodruff, T. Yang, L. Yates, G. P. Zeller, J. Zennamo, and C. Zhang. Determination of muon momentum in the MicroBooNE LArTPC using an improved model of multiple Coulomb scattering. *Journal of Instrumentation*, 12:P10010, October 2017. doi: 10.1088/1748-0221/12/10/P10010.

[59] V. L. Highland. Some practical remarks on multiple scattering. *Nuclear Instruments and Methods*, 129:497–499, November 1975. doi: 10.1016/0029-554X(75)90743-0.

[60] B. Gottschalk, A.M. Koehler, R.J. Schneider, J.M. Sisterson, and M.S. Wagner. Multiple coulomb scattering of 160 mev protons. *Nuclear Instruments and Methods in Physics Research Section B: Beam Interactions with Materials and Atoms*, 74(4):467 – 490, 1993. ISSN 0168-583X. doi: https://doi.org/10.1016/0168-583X(93)95944-Z. URL http://www.sciencedirect.com/science/article/pii/0168583X9395944Z.

[61] P. Abratenko and et al. Determination of muon momentum in the MicroBooNE LArTPC using an improved model of multiple Coulomb scattering. *Journal of Instrumentation*, 12:P10010, October 2017. doi: 10.1088/1748-0221/12/10/P10010.

[62] Tom Roberts. G4beamline User's Guide. Technical report, 12 2013.